Journal Pre-proofs

Major and trace element and multiple sulfur isotope composition of sulfides from the Paleoproterozoic Surda copper deposit, Singhbhum Shear Zone, India: Implications for the mineralization processes

Sangita Chowdhury, Dipak C. Pal, Dominic Papinue, David R. Lentz

Major and trace element and multiple sulfur isotope composition of sulfides from the Paleoproterozoic Surda copper deposit, Singhbhum Shear Zone, India: Implications for the mineralization processes

Sangita Chowdhury [a, †*], Dipak C. Pal[b], Dominic Papinue[c, d], David R. Lentz[e]

[a]*Departmant of Geology, University of Calcutta, Kolkata 700 019, India,*

[b]*Department of Geological Sciences, Jadavpur Universitty, Kolkata 700 032, India,*

[c]*Department of Earth and Environmental Sciences, Boston College, Chestnut Hill, MA 02467, United States,*

[d]*London Centre for Nanotechnology, Department of Earth Sciences, & Centre for Planetary Sciences, University College London, London, WC1H 0AH, United Kingdom*

[e]*Department of Earth Sciences, University of New Brunswick, Fredericton, New Brunswick E3B5A3, Canada*

[†] Corresponding author : e- mail: sangitageol@rediffmail.com

[*] Present address: Department of Civil Engineering, Dream Institute of Technology, Kolkata 700053, India

A B S T R A C T

The present study combines major and trace element composition, and sulfur (S) isotope data of pyrite and chacopyrite from the Surda copper sulfide deposit in the Singhbhum Shear Zone, the most important copper and uranium producing belt (Singhbhum Cu-U Belt) in India. Three textural and compositional types of both pyrite and chalcopyrite were distinguished; unzoned to partially zoned Pyrite IA with high Co (up to 54900 ppm) and low Ni content is earliest, followed by oscillatory zoned Pyrite IB with high As (up to 25600 ppm) and Co (up to 46800 ppm), bothoccurring in pyrite I + chalcopyrite I + pyrrhotite + magnetite + apatite vein; Cobaltite-type substitution $(Fe_{1-x}Co_x)(S_{1-x}As_x)_2$ is suggested for Pyrite IB. Gold occurs in Pyrite I as minor "invisible" gold and as electrum inclusions. It also occurs along with Cu, Mn, Ni, Hg, Ag, Pb, Sb, Zn, Ce, Y, U, and Th in micro-fractures that transgress the primary zoning pattern defined by As, Co, and Ni in Pyrite IB. The early inclusion-rich chalcopyrite generation (Chalcopyrite I) contains high concentration of Zn and Se, and minor to trace amounts of Co, Ni, Hg, Pb, Sb, Te, and Bi, appeared in between Pyrite I and II.Low Co, high Ni (up to 37700 ppm) content Pyrite II, and inclusion-free Chalcopyrite II enriched in Co, Ni, Hg, Bi, Mn, Ag, Sb, V, and Pb are cogenetic, and occurring in pyrite II + pyrrhotite + pentlandite + chalcopyrite II ± violarite vein.

Low Co and Ni containing Pyrite III + Chalcopyrite III occur mainly as disseminated grains. The relative timing of formation of Pyrite II + Chalcopyrite II with PyriteIII + Chalcopyrite III remains uncertain.

Pyrite + chalcopyrite textures indicate that all pyrite + chalcopyrite formed at some time prior to the end of deformation and metamorphism.

Both *in situ* and mineral separates of all pyrite types and associated chalcopyrite yield a narrow range of positive $\delta^{34}S$ values (between +3.8 to +6.9 ‰) suggesting sulfur being derived from a similar source. Consistent positive $\delta^{34}S$ values and other circumstantial evidence indicate that most sulfur was derived from seawater sulfate or modified seawater (brine/evaporite). $\Delta^{33}S$ values revealed mass dependent fractionation (MDF) signature. It is proposed that incorporation of MDF sulfur of the mineralization event in Paleoproterozoic Singhbhum Cu-U Belt took place after the great oxidation event. The high Se concentrations (260 to 400 ppm) and $\sum Se/\sum S$ ratios for both Pyrite I and II from Surda deposit (4.4 to 5.7 x10^{-4}) suggest a low temperature of the Cu–rich ores (250°-350°C), and precipitation from a metalliferous fluid with a high $\sum Se/\sum S$ ratio (10^{-4} to 10^{-3}) consistent with igneous input of these elements.

Keywords: Sulfide composition; sulfur isotopes; Surda copper deposit; Singhbhum Shear Zone; mineralization processes

1. Introduction

The Singhbhum Shear Zone (SSZ), a ~200 km long arcuate-shaped mineralized belt (also known as Singhbhum Cu-U Belt), occurs in the eastern part of the Indian Precambrian Shield. It is a well-known repository of copper, uranium, and apatite-magnetite mineralization (Sarkar, 1984). The large Surda Cu deposit is located in the eastern part of the SSZ.

This Cu deposit is hosted in highly deformed and hydrothermally altered rocks. Although the origin of the Surda and other deposits in the SSZ is thought to be hydrothermal in origin, the source(s) of hydrothermal fluid, sulfur, and metals, and the physico-chemical evolution of the sulfide minerals in the Surda deposit remain undetermined. Ore genetic models concerning the polymetallic mineralization in the SSZ have varied from a magmatic-hydrothermal origin (Dunn and Dey, 1942), metamorphogenic origin related to migmatization (Banerji, 1962; Talapatra, 1968), a sequence of geological processes that included intense shearing, syntectonic granitization and mobilization of the ore elements (Ghosh, 1972), variants of volcanogenic massive sulfide origin (VMS; Sarkar and Deb, 1974; Sarkar, 1984) to Fe oxide-Cu-Au (IOCG) type origin (Pal et al., 2009, 2010, 2011a, b).

Most of the sulfides typically have undergone ductile deformation, solid state or chemical remobilization, and annealing during dynamic metamorphism. However, pyrite can record and retain

the physical and chemical imprints of a sequence of events during and post-dating mineralization, even when subjected to high-grade metamorphic conditions (Barton, 1970; Craig and Vokes, 1993; Craig et al., 1998; Clark et al., 2004; Pal et al., 2009), but pervasive recrystallization in the presence of hydrothermal fluids can alter its primary composition (*cf*. Large et al., 2014). Optical microscopic examination and electron microprobe chemical mapping of pyrites from several deposits reveal that pyrite frequently contains both physical and chemical textures that may be interpreted in terms of the depositional and the post-depositional history of the deposits (Chowdhury and Lentz, 2017; Clark et al., 2004; Cook, 1996; Cook et al., 1994; Cox, 1987; Pal et al., 2009, 2011b). Thus, both physical and chemical intergranular relations and textures of pyrite may yield considerable information on the paragenetic history of an ore, as well as the chemical evolution of pyrite during the complex history of metamorphosed ores. Apart from the texturally-controlled chemical variation, the physico-chemical conditions of ore deposition directly influence the chemical characteristics of saturating pyrite (*cf*. Dehnavi et al., 2018).

Major, minor, and trace element contents of pyrite (Co, Ni, As, Se, Au, Cu, etc.) have potential to determine conditions of ore formation and to discriminate different classes of ore deposits (Pal et al., 2009 and references therein). Chemical mapping of elements, such as Ni, Co, and As, in pyrites reveals information on the relative time of transport of these elements in the ore fluids (Clark et al., 2004), and their possible redistribution during metamorphism. The preservation of textures and distinct trace element distribution patterns are often important evidence for multi-stage genetic development of an ore deposit (Fleet et al., 1993; Kouzmanov et al., 2002). Different pyrite generations can assist in the identification of sequential stages of mineral growth within multiphase or overprinted mineral growths (Cook et al., 2009; Large et al., 2007, 2009; Winderbaum et al., 2012).

The present study targeted a better petrographic, mineralogical and geochemical understanding of Surda pyrite and chalcopyrite with the objective of placing additional constrains on ore genesis. Compared to other common sulfides, there has been relatively minimal research of the ability of chalcopyrite to incorporate trace elements. An understanding of trace element chemistry of associated chalcopyrite is necessary to identify whether similar mineral-chemical signatures are present. Multiple S isotope compositions, including ^{32}S, ^{33}S, and ^{34}S, of sulfides provide key information to constrain the possible sources of S at the time of deposition. Most Archean sedimentary sulfides show $\delta^{34}S$ values near that of the mantle, whereas variability in primary $\delta^{34}S$ of sulfides may be modified during regional metamorphism and/or hydrothermal alteration. Therefore, $\delta^{34}S$ data alone does not unambiguously constrain the sulfur (or metal) source. $\Delta^{33}S$ values can provide a unique signature for the source of S, as the products of non–mass-dependent fractionation of S isotopes by photochemical reactions in the Archean oxygen-free atmosphere—oxidized water-soluble sulfur species with negative $\Delta^{33}S$ values, and reduced sulfur species with positive $\Delta^{33}S$ values can be readily distinguished from mantle-derived magmatic sulfides (*cf*. Bekker et al., 2009).

It, therefore, stands to reason that the source of hydrothermal fluids and the physico-chemical evolution of sulfide mineralization in a deformed and metamorphosed terrain can be better revealed integrating textures, chemical compositions (major, minor and trace element concentrations), and multiple sulfur isotope compositions of pyrite.

The aims of the present study are as follows:

1) To document the detailed textures of pyrite, and provide probable explanations for textural diversity.

2) To obtain detailed *in situ* trace element compositions and generate element distribution maps of selected elements for pyrite and chalcopyrite using both electron probe micro analyzer (EPMA) and laser ablation inductively coupled plasma mass spectrometer (LA-ICP-MS) for a better insight into the chemical evolution of mineralizing fluids.

3) To obtain *in situ* multiple sulfur isotope (δ^{34}S and Δ^{33}S) compositions of selected sulfide minerals using secondary ion mass spectrometer (NanoSIMS), and isotope ratio mass spectrometer (IRMS; using microdrilled sulfide samples) for the determination of source of sulfur for sulfide mineralization.

4) To integrate texture and composition (trace elements and isotopes) for a better understanding on the relative timing and mechanism of pyrite formation, chemical evolution of mineralizing fluids, and the source of sulfur/fluid.

2. Geologic background

2.1. Regional Geology

The Singhbhum Shear Zone (SSZ), ~200 km long and ~1–5 km wide, eastern India occurs close to the boundary between the Archaean granite-greenstone terrain on the south and the Proterozoic North Singhbhum Mobile Belt on the north (Bhattacharya and Mahapatra, 2008; Fig. 1A). The southern crustal province consists of the Iron Ore Group (IOG) (~ 3.5 Ga, Mukhopadhyay et al., 2008; Sengupta et al., 1994), and the Singhbhum Granite Batholith (SBG) Complex (~3.44-3.05 Ga, Acharyya et al., 2010), the later contains enclaves of Older Metamorphic Group (OMG) and Older Metamorphic Tonalittic Gneiss (OMTG). The supracrustal rocks that occur along the northern, western, and eastern margins of the craton, and include Paleoarchean Banded Iron Formations, are part of the IOG. The Chottanagpur Granite Gneissic Complex (CGGC) occurs to the northern margin of the SSZ. The mobile belt is represented by siliciclastic rocks belonging to Singhbhum Group and intercalated Proterozoic volcano-sedimentary rocks of the Dhanjori Group (lavas in its upper part, which were dated at ~2.10 Ga by Roy et al., 2002), and Dalma volcanic belt.

The SSZ cuts across the rocks of the Iron Ore Group, the Singhbhum Group, and the Dhanjori Group. Base-metal mineralization along with uranium mineralization occurs for about 60 km in the southeastern part of the SSZ, and hence, the SSZ is also known as Singhbhum Copper (Cu)-Uranium

(U) Belt. It has been suggested that the major phase of shearing and the final phase of tectonothermal event occurred at ~ 1.67-1.63 Ga (Sarkar et al., 1985; Sengupta et al., 1994, whole-rock Rb-Sr age), followed by a reactivation at around ~1.0 Ga (Acharyya et al., 2010a; Bose, 2009; Pal et al., 2011 a; Pal and Rhede, 2013; Sarkar et al., 1969, Sengupta et al., 1994). Recent studies of EPMA chemical dating of metamorphic monazite, indicate that the rocks of the North Singhbhum fold belt, of which the SSZ is a part, were affected by a metamorphic event between 1.7 to 1.5 Ga (Chatterjee et al., 2010; Mahato et al., 2008; Pal et al., 2011a; Rekha et al., 2011). The SSZ consists of quartz–biotite-chlorite schist, biotite-chlorite-quartz schist, mica schist (muscovite-biotite schist), tourmalinite, and bands of ferruginous quartzite (commonly with magnetite). These rocks have been affected by extensive albitization, biotitization, chloritization, and sericitization. Albite metasomatism has given rise to zones of albite schists and gneisses. These Na-rich rocks have been named as "soda granite" (Dunn and Dey, 1942), and dated by Sarkar et al. (1986) at 1.67 Ga (whole-rock Rb-Sr age), and at ~2.22 Ga and ~2.02 Ga (whole-rock Pb-Pb two-stage model age). According to Johnson et al. (1993), sulfide mineralization took place at ~1.77 Ga (Pb-Pb sulfide age). The end of tectonic activity in SSZ is marked by post-shearing faults. According to Sengupta and Ghosh (1997), the progressive deformation of the SSZ involved the initiation of a mylonitic foliation, its deformation by three generations of reclined folds, and superposition of two later groups of gently plunging asymmetric folds, and gentle and open upright folds. The total displacement along the SSZ was through a series of displacements along numerous mesoscopic shear zones.

The SSZ rocks underwent prograde metamorphism (M_1) that culminated in epidote-amphibolite facies, and that accompanied and outlasted this progressive deformation. The peak metamorphic P–T conditions estimated from mineral assemblages in pelitic rocks of the SSZ is 480±40°C and 6.4±0.4 kbar (Sengupta et al., 2005). Retrograde metamorphism (M_2) took place near the peak metamorphic temperature. It postdated ductile shearing, and took place during or after the waning stages of deformation (Sengupta et al., 2005).

The Singhbhum Cu-U Belt coincides spatially more or less with the SSZ, and an important source of Cu and U in India. This belt also contains economic deposits of apatite, magnetite, kyanite, and gold, silver, molybdenum, tellurium, which are recovered as byproducts of Cu- and U-mining. Mineralization in this belt has been known since ancient times, as evidenced by numerous old workings, ancient pits and slag heaps scattered along the belt in this area. Captain J. C. Haughton rediscovered copper in Singhbhum in 1854 (Dunn, 1937). After the preliminary work of Ball (1870) in this area, a detailed account of the mineralization of the Singhbhum Cu-U Belt was given by Dunn (1929, 1937) and Dunn and Dey (1942). Copper mineralization took place at many places along the SSZ confined to a zone up to 120 m wide, but concentrated only locally to constitute economic-subeconomic mineral deposits (Fig.1A). Economic deposits are located at Badia-Mosaboni, Pathargora, Surda, Kendadih, and Rakha mines.

2.2. Local Geology and Mineral Deposits at the Surda Mine

The Surda copper deposit is located in the eastern sector of the SSZ, and at the northwestern fringe of the Dhanjori basin. It occurs near the boundary between the volcano-sedimentary rocks of the Dhanjori Group and the predominantly siliciclastic rocks of the Singhbhum Group (Fig. 1A).

The rock formations in the area of the Surda deposit are regionally metamorphosed sediments and metavolcanics of Proterozoic age, which include epidiorite and basic rocks of Dhanjori Group, mica schist, kyanite- quartz rock, feldspathic schist, quartz-biotite-chlorite schist with tourmalinite, apatite, and magnetite ("granular rock"), biotite-chlorite-quartz schist, biotite schist, and quartzite (Dhanjori Quartzite) (Fig. 1B). The biotite-chlorite-quartz schist forms a continuous unit within the quartz-biotite-chlorite schist, and is the host unit for the bulk of Cu ore mineralization. Lenticular patches of mafic bodies are locally present in this unit. Quartz is the predominant mineral with varying proportions of chlorite. Other minor phases include biotite, magnetite, uraninite, tourmaline, Na-rich feldspar, apatite, epidote, allanite, and joisite. The rocks within the shear zone are highly sheared and mylonitized.

The regional strike of rock formations is N 10^0 to 40^0 W, and the dip is 20^0 to 60^0 towards NE. The shear zone maintains a NW-SE trend in this part of the belt. Within the shear zone the rock formations are folded into a series of major plunging folds and axes trending approximately ESE-WNW. The quartzite rocks show well-developed joint patterns. Three mutually perpendicular tension fracture systems and two diagonal shear fracture systems are observed in the host rocks. The linear structure in this area is represented by (i) pebble elongation, (ii) slickensides, (iii) parallel alignment of mineral grains, and (iv) axes of micro-folds. The pitch of the lineation is 45^0 to 50^0 towards N 50^0 E.

Both Cu and U mineralization in the Surda Copper Mine occur as lenses or irregularly-shaped masses of varying sizes generally nearly concordant to the schistosity of the host rock. The chlorite-biotite-quartz schists commonly contain significant amounts of apatite and magnetite. Within and along the shear zone narrow lenses of abundant mineralization are described as 'lodes'. In the southern part of the Surda Mine, there are three lodes, namely- the hanging wall, the intermediate, and the footwall. In the central and northern parts, number of shoots with intervening lean zones has formed lodes up to 20 m wide at places, which allows for bulk mining. The average width of lodes in the mine is about 6.6 m. The hanging wall lode is the richest in the mine block. Copper mineralization in the Surda area is also exposed on the surface of the hill slopes in the form of oxidized outcrop, and feeble gossan zones traceable along the strike of the formation. The depth of oxidation does not exceed 30 m, and the main minerals of the zone of oxidation are azurite, malachite, iron oxides and oxyhydroxides, which occur as stains on outcrops.

The Surda Copper Mine (22^0 $33^/$ $45^{//}$:86^0 $26^/$ $15^{//}$) of Monarch Gold [Contractor of Hindustan Copper Limited (HCL), a Central Public Sector Undertaking Company, and subcontractor- Indian Resource

Limited (IRL)] is located in the eastern sector of the SSZ (Fig. 1A). It is large Cu mine in India as it contributes more than 31% of the Cu reserves of the country. Production level is around 40,000 tonnes of Cu per year and daily production is around 500 tonnes. The ore developed along strike for around 2.3 km, with a maximum of 3.5 km at the 5th level in the mine, and a maximum depth of about 500 m at the 13th level. The reserve of Cu ore is 26.09 million tonnes at a grade of 1.20% Cu. The mineable reserve is 5.04 million tonnes at an average grade of 0.95% Cu (unpublished report of Hindustan Copper Limited, 2002-2003).

3. Sampling and Analytical techniques

Samples for this study were collected from all three lodes, namely the hanging wall, the footwall, and the intermediate lode (ores and mineralized host rocks), as well as along cross-cuts (unmineralized wall rocks) in the underground mine (from 3rd level to 10th level- 130m to 430 m from surface) (Fig. 1C). Sulfide-bearing metabasic rock samples were collected from the surface. Mineralogical and textural studies were carried out on 60 polished thin sections by optical microscope and on 10 selected sections by Scanning Electron Microscope (SEM).

For studying deformational and metamorphic features in pyrite and chalcopyrite, both Pyrite I and II are etched with H_2O_2 and concentrated HNO_3 for about 30 minutes, and both Chalcopyrite I and II are etched with saturated chromic acid solution, or a mixture of H_2O_2 and NH_4OH in the proportion of 1:1 for about 40 to 60 minutes.

Pyrite grains in the samples chosen for analysis were characterized using optical and backscattered electron (BSE) imaging with a JEOL JSM-6400 Scanning Electron Microscope housed in the Microscopy and Microanalysis Facility, University of New Brunswick, Canada (UNB). The compositions of both pyrite and chalcopyrite were determined using EPMA and LA-ICP-MS. Element distribution maps of entire or part of some selected grains were generated using both EPMA using a JEOL JXA-733 Superprobe, and LA-ICP-MS using Laser at UNB. Minimum detection limit for EPMA analyses is at $\pm 2\sigma$ (95% confidence interval). Optimum detection limits for Co is 250 ppm, for Ni 260 ppm, for Cu-300 ppm, for As 220 ppm, and for Se 190 ppm.

Sulfur isotope analyses ($\delta^{34}S$) were performed with a Cameca NanoSIMS 50L at the Carnegie Institution of Washington (Hauri et al., 2016) on pyrite and chalcopyrite grain separates mounted in indium metalPrecision with the nanoSIMS for $\delta^{34}S$ was better than 0.02‰, and the 2-σ reproducibilities for $\delta^{34}S$ were ± 0.47‰.

Multiple S isotope measurements by IRMS were performed at Boston College and Harvard University using an elemental analyzer (EA) coupled to an IRMS in continuous flow mode using the SO-SO_2 method (Baublys et al., 2004). Precision on standard SO_2 gas for $\delta^{34}S$ was better than 0.02‰

(1σ, n = 8 peaks), and the average 1σ reproducibilities for all standards used were 0.3, 0.4, and 0.2‰ for $\delta^{33}S$, $\delta^{34}S$, and $\Delta^{33}S$, respectively.

The detailed procedures of SEM- BSE imaging, EPMA and LA-ICP-MS analyses, multiple S isotope measurements by NanoSIMS and IRMS are included in the Supplementary material (Appendix A).

4. Results

4.1. Mode of occurrences and textures of pyrite, chalcopyrite and associated sulfides

The mode of occurrences and textures of pyrite and associated sulfides were deciphered using hand specimen study and optical (reflected and transmitted) microscopy and back scattered electron imaging (BSE).

4.1.1. *Mode of occurrence*

In the Surda deposit, chalcopyrite is the most abundant sulfide mineral. Pyrite is also abundant and common after chalcopyrite, which is followed by pyrrhoytite, and accompanied by magnetite, ilmenite, and minor pentlandite, molybdenite, violarite, bravoite, and uraninite. Pyrite content in the deposit varies from 2 to 5 vol. %, whereas outside the deposit, the pyrite content is generally less than 1 vol. %. Within the ore zone and in the wall rocks pyrite and chalcopyrite occur primarily in mineralogically diverse massive sulfide veins that parallel the pervasive foliation (Fig. 2A) and less commonly as disseminated individual grains and clots of composite aggregates in the silicate matrix. Occasionally thicker sulfide bands (chalcopyrite) appear co-folded with the host schists along with flowage features showing concentration of sulfides in crests and troughs, and also thinning of sulfide layers in the limb regions of micro-folds (Fig. 2B). Pyrite in the sulfide veins generally occurs in three mineralogically different associations: Concordant veins of 1) pyrite I + chalcopyrite I + pyrrhotite + magnetite + apatite (Type I vein) (Fig. 2C), and 2) pyrite II + pyrrhotite + pentlandite + chalcopyrite II ± violarite (Type II vein) (Fig. 2D), and disconcordant veins of 3) pyrite+ pyrrhotite + pentlandite + chalcopyrite + violarite + bravoite ('bravoite' is termed as Nickeloan pyrite/ Ni-pyrite; Bayliss, 1989; Harms, 2009; henceforth the term 'Ni-pyrite' will be used in this article) (Type 3 vein). Discordant Type 3 veinlets also occur within chalcopyrite (Fig. 2E). In addition to pyrite-bearing veins, disseminated Pyrite III grains (Fig. 2C) occur in the host rock. It is to be noted that the discordant veins and veinlets are restricted only at the shallow levels of the Surda mine (up to 5th level- 230 m from surface) and interpreted to be supergene in origin (Section 5.3. Nickel Pyrite (Bravoite) and Nickel-bearing Pyrite). Consequently, in subsequent sections only the detailed textures and geochemistry of Pyrite I to Pyrite III are described and their

implications discussed. Table 1 summarizes the salient textural and compositional characteristics of Pyrite I to Pyrite III.

4.1.2. *Textures*

Based on mode of occurrence, texture and mineralogical association, pyrite and chalcopyrite in the Surda deposit are classified into three types-1) anhedral to subhedral (0.01-0.5 mm) (Fig. 3A) and euhedral (Fig. 3B) Pyrite I grains + inclusion-rich, massive Chalcopyrite I grains occurring in Type I vein; 2) subhedral and fractured Pyrite II+ cleaner, inclusion-free xenomorphic to hypidiomorphic aggregates of Chalcopyrite II grains widely varying in size in Type 2 vein; and 3) idiomorphic Pyrite III + xenomorphic inclusion-poor Chalcopyrite III occurring mainly as disseminated grains (Table 1). Pyrite I occurs in both massive ore and wall rocks particularly in chlorite schist and muscovite-chlorite-biotite schist. These Pyrite I grains are fractured, and the fractures are commonly filled by both Chalcopyrite I and II (Fig. 3C and D). Fractures are not always oriented and show cataclastic deformation. The idiomorphic and relict individual Pyrite I, and monomineralic pyrite clusters occurring along small discontinuous layers are embedded in Chalcopyrite I groundmass (Fig. 3D). All the above features indicate that Pyrite I appeared probably earlier than Chalcopyrite I. Some grains of Pyrite I contain inclusions of uraninite (Fig. 3E). The small polygonal to rounded Pyrite I grains are inclusion-free. In some schistosity-parallel veins, pyrite is locally elongate in nature (Fig. 3F) with its long dimension parallel to the mylonitic foliation of the host schist (Fig. 2C). The size of these grains ranges between 0.8 to 2 mm. They do not have well-developed crystal habits and contain fractures perpendicular to the direction of elongation. Anhedral to rounded magnetite grains occur in both subhedral and elongate grains. The magnetite inclusions give rise to higher magnetism of some of the pyrites. The etched polygonal to rounded, inclusion- free Pyrite I locally shows growth and annealed texture, with few grains showing triple-point junctions (Fig. 3G). Relicts of subhedral to euhedral grains (2 mm) of magnetite occur within Chalcopyrite I. The fractures of magnetite are also filled by Chalcopyrite I. All these evidences indicate that Chalcopyrite I formed after magnetite. Pyrrhotite and pentlandite occur as veinlets into Chalcopyrite I grains (Fig. 3H and I) indicating their formation after the formation of Chalcopyrite I. Molybdenite occurs within or around Chalcopyrite I grains (Fig. 3H). Sub parallel arrangement, worm-like and needle-like grains of mackinawite within Chalcopyrite I suggest that mackinawite has exsolved from Chalcopyrite I.

In the mineralized zone, Pyrite II is found in association with Chalcopyrite II, pyrrhotite, pentlandite, and violarite (Fig. 4A-D). The pyrite grains are composite and fractured. The etched Pyrite II grains reveal sub-grains (Fig. 4E), and intergranular fractures. Stumpy subhedral grains of pentlandite occur with Pyrite II. Violarite occurs along the fractures, and replace Pyrite II along the rim (Fig. 4C and D). It also occurs as fringes along late fractures and as well-developed replacement fronts inward from the grain margins of pentlandite. Violarite displays poor polish with a distinctive mottled or pitted

appearance in reflected light (Fig. 4F). Microfractures are abundant in coarser violarite aggregates. Upon exposure to air, polished aggregates of violarite tarnish rapidly. These violarites typically yield low analytical totals in EPM analysis (~96%; Table 2). Pyrite II commonly contains inclusions of magnetite (Fig. 4A). Small rounded pyrite grains (0.01-0.02 mm) occur as inclusion in Chalcopyrite I. Subhedral Pyrite II (0.2-0.5 mm) contains rounded inclusions of Pyrite I and poikiloblastic inclusions of Chalcopyrite II (Fig. 4B). Chalcopyrite II and Pyrite II show straight and mutual boundary relationship (Fig. 4A) indicating simultaneous crystallization of both the minerals, while Chalcopyrite II also occurs along the fractures of Pyrite II indicating later formation of Chalcopyrite II than Pyrite II. All these evidences indicate that Chalcopyrite II started to crystallize along with Pyrite II, and continued to precipitate after the formation of Pyrite II. Common tounge like projection of Chalcopyrite II into pyrrhotite indicates their formation after the formation of pyrrhotite. Chalcopyrite, which shows massive appearance without any grain outline in polished sections, after etching gives rise to small and large crystals with distinct grain boundaries. The presence of small grains with local bent boundaries in Chalcopyrite I is also not uncommon. Etching also reveals different types of twinning like "polysynthetic type", which are continuous and "chevron type" with long and short limbs. The lamellae are both lanceolate to spindle shaped and parallel- sided. The parallel- sided lamalle may be continuous across the entire grain or may terminate abruptly within it (Fig. 4G-I)

Pyrite III forms very small disseminated euhedral to rounded grains (Fig. 2C) in the host rock as well as wall rocks. Euhedral Pyrite III overgrows on Pyrite I (Fig. 4J and K). Pyrite III shows foam-like triple point junction (Fig. 4L). A third generation of minor Chalcopyrite III is cogenetic with Pyrite III showing mutual boundary relationship with each other (Figs. 4J and L).

4.2. Major and trace element geochemistry of pyrite

Compositions of pyrite in the Surda deposit show systematic variations that correlate well with their mode of occurrences, textures, and mineralogical associations (Tables 1-3, and Supplementary materials, Appendices B. 1.-B. 18. for the full EPMA and LA-ICP-MS dataset of pyrite and chalcopyrite). The overall pyrite composition exhibits considerable spread in the Fe versus S plots, and deviates from the ideal cation to anion ratio (Fe = 46.6 wt.% and S = 53.4 wt.%) of stoichiometric pyrite (Fig. 5A). Among the minor elements analyzed, Co and/or Ni are detected in most grains of pyrite, and As is recognized in some pyrite grains.

There are systematic differences in the concentration of Co and Ni (Fig. 5B) in three different textural types of pyrite described in earlier section. The individual pyrite grains from different types also show variations in Co and Ni concentrations from core to rim, which make these two elements useful in correlating textural and compositional types and tracing the compositional evolution of pyrite.

Chemical variations in the Pyrite I grains detected by EPM analyses and X-ray element mappings by both EPMA and LA-ICP-MS methods allowed the identification of two subgroups in Pyrite I.

Pyrite IA shows unzoned and partially zoned pyrite with high Co (up to 54900 ppm), no or bdl (below detection limit) of As (dl; detection limit 220 ppm), and Ni [bdl (dl 260 ppm) to 2500 ppm], Co/Ni ratios ranging between 0.24 to 94.

Pyrite IB displays oscillatory-zoned pyrites with high Co (5300 to 46800 ppm), As (bdl to 25600 ppm), and Ni (bdl to 1200 ppm), Co/Ni ratios ranging between 0.15 to 100.

Pyrite II shows moderate to very low (400 to 8700 ppm) to bdl Co (detection limit 250 ppm), Moderate to high Ni (1200 to 37700 ppm), Co/Ni ratios ranging between 0.05 and 0.58.

Pyrite III shows low Co (300 to 600 ppm), Low (300 to 1200 ppm Ni) to bdl Ni, Co/Ni ratio ranging between 0.40 and 0.70.

4.2.1. Pyrite I

Pyrite IA is more abundant than other pyrite types. Overall Co and Ni contents decrease from Pyrite IA to Pyrite IB, while in both Pyrite IA and Pyrite IB, Co content decreases from core to rim, while Ni content shows slight increase towards rimin Pyrite IA, and As content decreases from core to rim of Pyrite IB. Inverse correlations exist between Co–Fe (Pearson's correlation coefficient, r = - 0.90), Ni-Fe (r = - 0.48), and As-S (r = - 0.86) (Fig. 5C-E). In each well-defined zone, the Co and As content are quite uniform. The As enrichments show positive correlation with Co enrichments (r = + 0.87) (Fig. 5F). Pyrite IA (13200 ppm Co) occurs as inclusion within Ni-rich pyrrhotite (3500 ppm Ni), which is replaced by Ni-pyrite and in places contains inclusions of bismuth telluride. Pyrite IA contains higher contents of Co and lower contents of Ni compared to coexisting pyrrhotite (Fig. 6A; Table 2). Some Pyrite IA grains show localized and partial zoning of Co, while some other grains are compositionally homogeneous. The homogeneous Pyrite IA grains show high Co throughout the grain. The compositionally heterogeneous Pyrite 1A grains (Fig. 6B) show compositional zoning between core and rim with cores up to 54900 ppm Co, and below detection limit Ni, and rims up to 24600 ppm of Co, and 2500 ppm of Ni (Fig. 6C-E; Table 2). X-ray element mapping of a Pyrite IA grain (Fig. 6B) shows localized zoning with Co rich rugged core that does not mimic the grain shape, while successive growth zones are symmetric and follow the external morphology of the grain (Fig. 6C). Individual large porphyroclastic and small euhedral to subhedral Pyrite IB grains (Fig. 6F) commonly exhibit compositional zoning with cores up to 46800 ppm Co, 25600 ppm As, and rims up to 30000 ppm of Co, with bdl As. Cobalt and As contents decrease from core to rim (Fig. 6G and H; Table 2), while a thin layer of Ni occurs along the rim (Fig. 6I). This grain (Fig. 6F) partly includes epidote, and the contact between pyrite and epidote is depleted in Co and As (Fig. 6G and H). A couple of analyzed points in the core of this pyrite grain show very low concentrations of Co, which is likely due to the presence of fractures at these points, while locally some points show high concentration of Co and Ni

which may be due to sub-microscopic inclusions (Fig. 6G and I). The euhedral boundaries of some Co- and As-rich zones which are sub parallel to the crystal faces are often concentric (Fig. 7A-F). Relic of the Pyrite IB (containing high concentration of Co and As) is present at the core of Pyrite III (Fig. 7G and H). The stretched Pyrite IB grains (Fig. 3F, Table 2) are also characterized by high Co contents (>10000 ppm) and distinct chemical zoning. Here also both Co and As contents decrease from core to rim. The zoning is not always sharp. In some cases, succession of different Co and As zones give the appearance of typical oscillatory-zoned pyrites (Figs. 6G- J, 7A-H). Chemical profile along a length of 1000 µm (Fig. 6J) shows the fluctuations in the absolute concentrations of Co and As throughout the Pyrite IB grain which can be correlated with fine oscillatory zoning. In the euhedral Pyrite IB Ni shows incipient reverse zoning with increased concentration of Ni towards rim (Fig. 7I-K).

Chemical composition determined by LA-ICP-MS shows high concentrations of Co and Ni in Pyrite IA, moderate to high and significant concentrations of As, Bi, Co, Cu, Mn, Ni, Pb, Sb, V, Se, U, Th, Ag, and Au in Pyrite IB, and very low concentrations of Zn, Mo, Cd, Ti, Sn, Ce, Y, and Te in both Pyrite IA and IB (Table 3). The LA-ICP-MS element distribution map shows overgrowth of As (up to 2000 ppm)-, Co (~0.94 wt. %)-, Ni (~1230 ppm)-, Se (up to 204 ppm)-rich Pyrite IB on Co- rich (up to 1.9 wt %), and As-, Ni-poor Pyrite IA. The boundary between the As-poor core and As-enriched zone are not idiomorphic, and are discontinuous without mimicing the grain shape (Fig. 8). In contrast, Fig. 9 shows Co (~1.7 wt. %)-, Ni (~600 ppm)-rich, As (~70 ppm)-poor core (Pyrite IA) have been truncated and overgrown by younger Ni (~100 ppm)-poor, Co (~1.4 wt. %)-, As (~1550 ppm)-rich Pyrite IB. The boundary between the As-poor core and As-enriched zone mimics the grain shape (Fig. 9). The Co and As LA- ICP-MS distribution maps also show partial and fine oscillatory zoning of Pyrite IB (Figs. 10, 11, and Supplementary material Appendix C). Gold (Au) occurs as dissemination throughout the Pyrite IB grain without showing any correlation with As (Fig.10). Most gold occur along fractures and grain boundaries of Pyrite IB, and are well-correlated with Cu, Mn, Ni, Pb, Sb, Ag, and Hg (Fig. 11).

Nickel has dual nature in both Pyrite IA and Pyrite IB, following the reverse zoning pattern defined by As and Co (Fig. 11 in Pyrite IB), homogeneous distribution (Fig. 8 in Pyrite IA), and also enrichment along cracks (Fig. 8 for both Pyrite IA and IB, and Fig. 11 for Pyrite IB). LA-ICP-MS maps of Pyrite IB show As, Co, Se and Ni variations defining fine-scale euhedral to subhedral boundaries (Figs. 10, 11). The cracks filled by Cu, Mn, Ni, Hg, Au, Ag, Pb, Sb, Zn, Ce, Y, U, and Th transgresses the zoning pattern defined by As, Co and perhaps Ni and Se. Bismuth and Te are positively correlated (Figs. 8, 10), and occurs along another set of cracks along with Cu and Zn also (Fig. 11). The relative timing relation between Bi-Te with Ag-Cu-Ni-Pb-Hg is unclear. Bismuth and Zn concentrations are low in some pyrite grains with an average value of ~ 4 ppm, while in others the concentrations are very high in the rim portion of Pyrite IB (with average value of Bi varies from ~ 200 to ~ 900 ppm, and with maximum concentration of Zn is 1073 ppm). The EPMA values of Se vary between 260 to 400 ppm. The average LA- ICP-MS Se value of Pyrite I is below 250 ppm. In both Pyrite IA and B, Se is broadly

12

correlated with Ni, and increases from core to rim (Figs. 8, 9, and Appendix C). In Pyrite IA, besides Co, Ni, and Se, trace amounts of Cu, Hg, V, Ti, and Zn are disseminated throughout the Pyrite IA grain. In this pyrite, As is very low (about 70 ppm), and Au, Ag, Bi, and Mn are totally absent (Fig. 9).

4.2.2. Pyrite II

Pyrite II has high Ni (6400 - 37700 ppm) and moderate Co (800 - 2100 ppm) contents (Fig. 5B). Pyrite II also shows compositional zoning represented by increasing Ni and decreasing Co content from core to rim (e.g. > 8000 ppm Ni and ~2000 ppm of Co at core and up to 37700 ppm Ni at rim, while Co is below detection limit to 1800 ppm). Pyrite IA inclusion in Pyrite II is characterized by moderately high Co (up to 8000 ppm) and bdl Ni. The included Chalcopyrite II contains about 1000 ppm of Co, while Ni content is 31000 ppm (Fig. 4B; Table 2). Pyrite II is replaced along grain margins and fractures by Ni-pyrite (Fig.4C, D) containing high Co (3.7 - 8.7 wt. % Co and 23 - 30 wt. % Ni), and by Ni-rich violarite (Fig.4C) containing 16.0 - 28.7 wt. % Ni (Table 1). A fractured Pyrite II grain (Fig. 12A) after X-ray element mapping shows heterogeneous distribution of Ni. Pyrite II is locally replaced by Ni- and Co-rich phases along micro-cracks, and also Ni-rich phases at the grain boundary (Fig. 12 B, C). These rims were too small to be analyzed, but may represent Ni-pyrite. Pyrite occurring along with pentlandite, pyrrhotite, violarite, and Ni-pyrite in veinlets at higher levels also contains moderate Ni (1200 ppm, Fig. 2E; Table 2).

4.2.3. Pyrite III

An anhedral Pyrite III grain (Fig. 4L) after elemental mapping does not show internal zoning, and is depleted in Co, As and Ni (Figs. 7G, H, L, 12D-F) compared to Pyrite I and II (both Co and Ni are below 700 ppm, and bdl As). Though Pyrite III contains bdl Se, in only one sample, Pyrite III has Se value of 3100 ppm (Table 2) which may be due to sub-microscopic inclusion. Pyrite III shows triple point junction (Fig. 4L), and is also replaced along grain boundaries and fractures, by Ni- and Co-rich Ni-pyrite (Fig. 12D and E).

4.3. Major and trace element geochemistry of chalcopyrite

4.3.1. Chalcopyrite I

The composition of Chalcopyrite I (Cu = 31 wt.% to 56 wt.%, Avg.= 31.36 wt.%, Fe = 32.6 wt.% to 33.1 wt.%, Avg.= 32.72 wt.%, S = 32.8 wt.% to 35 wt.%, Avg. 33.45 wt.%, and Cu wt.%/Fe wt.% = ~ 0.96) shows deviation from the ideal composition (Cu = 34.65 wt.%, Fe = 30.45 wt.%, S = 34.9 wt.%, and Cu wt.%/Fe wt.% = 1.14). The Co and Ni contents of this chalcopyrite usually vary between bdl to 0.05 wt.% and bdl to 0.04 wt.% respectively (Table 2).

LA-ICP-MS spot analyses of Chalcopyrite I (Table 3) reveals the presence of high concentrations of Zn (283 to 129 ppm, Avg. 205 ppm), Se (306 to 80 ppm, Avg. 185 ppm), and Pb (155 to 0.2 ppm). Bismuth (Bi), Co (up to 60 ppm), and Ni (up to 2290 ppm) are all commonly present at measureable levels, while Te, V, As, Cd, Mo, Mn, Ba, Sb present as trace amounts.

LA-ICP-MS trace element maps reveal homogeneous distribution of Fe, Cu, Zn, and Se, and disseminations of Co, Ni, Bi, Hg, and Pb in Chalcoyrite I. Unidentified Bi- (Fig. 13) and Mn-, Ag-bearing phases (Fig. 14) occur along microfractures of Chalcopyrite I. Gold (Au), As, and Mo are not detected.

4.3.2. *Chalcopyrite II*

The composition of Chalcopyrite II (Cu = 29.65 wt.% to 31.6 wt.%, Avg.= 31.37 wt.%, Fe = 32.26 wt.% to 32.93 wt.%, Avg.= 32.55 wt.%, S = 33.3 wt.% to 34.8 wt.%, Avg. = 33.96 wt.%, and Cu wt.%/Fe wt.% = ~ 0.92) shows deviation from the ideal composition. In Chalcopyrite II, Co is up to 0.1 wt.%, and Ni is up to 3.1 wt.% (Table 2).

LA-ICP-MS spot analyses of Chalcopyrite II (Table 3) reveal the presence of high to low concentrations of Zn (575 ppm to bdl, Avg. 174 ppm), Se (582 to 38 ppm, Avg. 170 ppm), Ni (14600 to 70 ppm, Avg. 2000 ppm), and Mo (246763 ppm to bdl, Avg. 4855 ppm). Lead (up to 4400 ppm; Avg. 62 ppm), Ag (up to 24 ppm, Avg. 10 ppm), Bi (up to 957 ppm), Te, V, Co, As, Cd, Mn, Ba, and Sb are all commonly present at measureable levels in Chalcopyrite II. In comparison with Pyrite I and II, both Chalcopyrite I and Chalcopyrite II are enriched in Zn, Pb, Mn, V, Cd, Sb, and Hg, and lower in concentration of Co, As, Se, Te, and Bi.

LA-ICP-MS trace element maps reveal overgrowth of Chalcopyrite II on Chalcopyrite I (Figs. 13, 14). In the maps, Co, Ni, Hg, Bi, Mo, Mn, Ag, Sb, V and Pb show increased concentrations towards rim of Chalcopyrite II, whereas Au and As occur in traces. The distribution of Ni closely mimics that of Co in both Chalcopyrite I and II, though Ni concentration in Chalcopyrite II is greater than Co concentration. The observed trace element distributions in chalcopyrite clearly show that the same elements occur as disseminations and in fractures of Chalcopyrite I are also present in the sulfide lattice of Chalcopyrite II at significant levels.

4.3.3. *Chalcopyrite III*

As Chalcopyrite III is a rare phase, so LA-ICP-MS trace element analyses and maps are not available. EPMA mapping of only Co, Ni, and As show absence of Co and Ni in Chalcopyrite III, while As occurs in trace amounts (Fig.12D-F).

4.4. *Multiple sulfur isotope compositions of pyrite and chalcopyrite*

Multiple sulfur isotope compositions were determined in Pyrite I, Pyrite II, Chalcopyrite I and Chalcopyrite II by Nano SIMS and IRMS methods (Tables 4 and 5). In general, sulfur isotope compositions of all Surda pyrite and chalcopyrite are consistently positive, and fall within a small range; $\delta^{34}S$ values vary from + 3.8 to + 6.2‰ by NanoSIMS method, and +5.4 to +6.8‰, by IRMS method. $\Delta^{33}S$ values determined by IRMS method vary between +0.60 and -0.20‰. The in situ S isotope investigations were carried out in the single grains of pyrite and chalcopyrite (Fig. 15). The analyzed Pyrite grains exhibit a slight intra-grain zonation of $\delta^{34}S$ values. These $\delta^{34}S$ values range from +3.9 to +5.7‰ in Pyrite I, +3.6 to +5.3‰, and +4.4 to +5.4‰ in Pyrite II within a distance of 400 μm and 100 μm (Fig. 15A-C) respectively. The $\delta^{34}S$ values of chalcopyrite are more homogeneous than that of pyrite (Fig. 15C and D). Within a distance of 100 μm, these values show a range from +4.9 to +5.1‰ in Chalcopyrite II (Fig. 15C), and from +4.2 to +4.7‰ in Chalcopyrite I (Fig. 15D). A single spot analysis of $\delta^{34}S$ in Chalcopyrite II (Fig. 15D) shows value of +6.2‰.

The lowest $\delta^{34}S$ values observed in Pyrite IA (3.9 to 4.6‰) correspond to Co rich core (1.03% to 1.5%). The low $\delta^{34}S$ and Co-rich core is overgrown by a high $\delta^{34}S$ zone (5.4 to 5.7‰) that is characterized by low Co content (0.9 to 0.7%) (Fig. 15A and E). There is no obvious correlation between the Ni values and S- isotopic variations (Fig.15B). The $\delta^{34}S$ values of micro-drilled powdered samples (EA-IRMS analysis) more or less tally with the results of NanoSIMS analyses of the same samples. Most of the micro- drilled powdered samples of pyrite and chalcopyrite showing $\Delta^{33}S$ values close to zero (Table 5), fall within the mass dependent S isotope fractionation (MDF) band.

5. Discussion

5.1. *Effects of ore deformation and metamorphism at Surda*

The effects of deformation and metamorphism are clearly recognized in the Surda ores as evidenced by the various fabric characteristics shown notably by chalcopyrite and pyrite. The flow- folding of the ore minerals mainly chalcopyrite and silicate gangue minerals (Fig. 2B), vein quartz, and the presence of shear planes in the ores are some of the megascopic features bearing testimony to the deformation that involved the ores of the Singhbhum Cu-U Belt. Veins and veinlets of chalcopyrite, and chalcopyrite-, pyrrhotite-rich ores were formed by plastic flowage. Petrographic study has shown extensive remobilization and fracture-filling of chalcopyrite in other minerals.

The evidences of deformation on chalcopyrite appear to be marked by slip lines, branched and curved twins, polysynthetic twins, and distorted twin boundaries (Fig. 4G-I). Twins in chalcopyrite formed during dynamothermal-dynamic metamorphism. From experimental studies on chalcopyrite deformation (Kelly and Clark, 1975), it has been suggested that at about 100^0C, deformation twinning becomes an important mechanism, and the strength of chalcopyrite is substantially reduced. The

presences of small grains with local bent boundaries in Chalcopyrite I indicate possible sub-grains. Local presence of foam-like triple point junctions indicates recrystallization of grains. Thus the present data suggest that the chalcopyrite-bearing ore at Surda has been subjected to deformation and metamorphism.

The morphology of elongated Pyrite I (Fig. 3F) and II (Fig. 4A) grains oriented along the host schist may have responded to dislocation flow (Cox et al., 1981), but also suggests that deformation by pressure solution might have taken place, a process very common in low-grade metamorphic terrains (Mc Clay and Ellis, 1984). The annealed texture of few Pyrite I grains (Fig. 3G) indicate recrystallization. Pyrite II grains reveal deformation textures like sub-grains (Fig. 4E), and intergranular fractures in Pyrite II. Arrays of pits in this pyrite form sub-grain walls, and indicate the onset of polygonization (Atkinson, 1975).

5.2. *Implications of trace- and major-element compositions of Surda pyrite*

5.2.1. *Cobalt, Nickel, and Arsenic in pyrite*

As concentrations of Co and Ni are not significantly modified during subsequent metamorphism and deformation, concentrations of these two elements, still show recognizable differences among the different pyrite types, although all identified pyrite types are metamorphosed. The concentration of Co and Ni in hydrothermal pyrite should largely depend on their concentration in the fluid, and perhaps on the oxidation state of Fe. According to Walshe and Solomon (1981), Co-rich pyrite may form in response to a drop in fO_2, and increase in pH accompanying chalcopyrite mineralization. Thermodynamic modelling of Co transport in hydrothermal fluids suggests that tetrahedral $CoCl_2^{-4}$ is the dominant Co carrying complex above 250°C, and in moderate to low salinity (6 m NaCl solution) (Liu et al., 2011; Migdisov et al., 2011). Furthermore, Liu et al. (2011) proposed that a drop in temperature and/or small drop in salinity of weakly saline hydrothermal fluids results in the decrease in the stability of $CoCl_2^{-4}$ leading to the precipitation of Co. High-Ni sulfide minerals are found in several ultramafic-hosted sites, where mineralization is related to the interaction of hydrothermal fluids with ultramafic basement, which contains higher Ni concentrations than mafic rocks (Fouquet et al., 2010; Keith et al., 2016).

In the Surda sulfide deposit, the decreasing concentration of Co from Pyrite IA to Pyrite III and Ni from Pyrite II to Pyrite III can be explained by various ways. The patchy and rugged Co-rich core (Fig. 6C) in some composite pyrite grains indicate that though the overall composition of this pyrite is that of Pyrite I, the early grain (Pyrite IA) was more enriched in Co, and was later replaced by a relatively less Co-rich pyrite (Pyrite IB). The sharp contact between Pyrite IA and Pyrite IB indicates that the replacement process was controlled by interface coupled dissolution and re-precipitation mechanism, overgrowths or grain clusters, and not by diffusive loss or gain of elements (*cf*. Eames et

al., 2016). A drop in pH and increase in $f\mathrm{O}_2$ resulting in a lesser amount of Co partitioning into pyrite can also explain the low Co content of Pyrite III.

However, Ni-poor Pyrite I is likely the result of primary low Ni concentrations in the hydrothermal fluids (Maslennikov et al., 2009), and Pyrite III is the result of depletion of Ni content in the late hydrothermal fluid. Pyrite II grains show compositional zoning represented by increasing Ni and decreasing Co content from core to rim (Table 1). The negative correlation between Co and Ni indicates that Co and Ni did not precipitate simultaneously during pyrite growth. Some euhedral to subhedral Pyrite III that overgrew Pyrite I (Fig. 4J) at Surda have moderately high Co- to- Ni ratios, compared to most Pyrite III. These pyrites might have crystallized/re-crystallized during metamorphism from existing pyrite with little or no addition of external materials.

Arsenic is generally considered to be incorporated into the pyrite lattice by substitution of reduced As^{1-} for S (Savage et al., 2000; Lowers et al., 2007). These substitutions should induce some changes in the crystalline lattice parameters. The ore assemblage at the Surda sulfide deposit reflects the reducing conditions of the fluid, so As^{3+} is minor. Besides, the negative correlation between Co - Fe (Fig. 5C), As - S (Fig. 5E), and positive correlation between Co and As concentrations (Fig. 5F) in arsenian pyrite (Pyrite IB) suggest that the substitution of S by As was accompanied by substitution of Fe by Co, which may lead to cobaltite-type $(Fe_{1-x}Co_x)(S_{1-x}As_x)_2$ substitution mechanism of Pyrite IB in which As^{1-} substitutes for S in the pyrite structure (Deditius et al., 2008; Fleet et al., 1993; Li et al., 2014; Reich et al., 2005). Arsenic mobility is often linked to Fe and S cycling at redox boundaries, apparently due to co-precipitation reactions of As with pyrite (e.g., Edenborn et al., 1986; Moore et al., 1988). According to Fleet et al. (1989, 1993) and Huston et al. (1995), As is incorporated in pyrite lattice as a metastable solid solution of the Fe (S, As) type, with a marcasite-like structure, and is usually expelled from pyrite during metamorphism. Ballantyne and Moore (1988) attributed it to a redox disequilibrium reaction between the As-bearing ore fluid and crystallizing pyrites. According to Pokrovski et al. (1996), at temperatures greater than 250°C, Fe-Co-Ni arsenides and sulfide-arsenides like As-bearing pyrite are formed. At Surda, the textural relationship of the As-rich pyrites suggest the possibility of a redox disequilibrium reaction between the As-bearing ore fluid and crystallizing pyrites is likely to account for the dominant occurrence of As-rich Pyrite IB core.

The As-rich zones define more or less as concentric zones in the Pyrite IB grains, which generally mimic the grain shape. However, in some cases, the presence of irregular boundaries, suggesting chemical overprinting by retrograde reaction or dissolution of older As-poor pyrite (Pyrite IA) before growth of As-rich pyrite (Pyrite IB) (*cf*. Franchini et al., 2015). The As-rich zones are also enriched in Co, but concentration of Co is less than that of Pyrite IA. The positive correlation between As and Co indicates that As and Co are intrinsic to Pyrite IB. The zonation in trace metals in some Pyrite IB defined by a Co-, As-rich core (Fig. 7G and H), which are also characterized by lower Fe and S than the average pyrite matrix. This feature indicates that As and Co are mainly incorporated in the pyrite structure, and

not as mineral inclusions. It is proposed that during pyrite growth, Co coprecipitates with As, and are localized in the Pyrite IB lattices. The relations of Co with As should, therefore, be a function of original concentration of these elements in the hydrothermal fluid, which itself is a function of temperature, salinity, fO_2, and fS_2.

There are several possible origins of oscillatory zoning in the individual Pyrite IB grains defined by the concentrations and alternations of microscale zones of Co and As (Figs. 6G, H, 7A-F): disequilibrium growth conditions resulting from episodic fluctuation in hydrothermal fluid conditions during crystal formation (Fleet et al., 1989), nucleation-induced oscillations in temperature (Brandles et al., 1984), diffusion-controlled process, an ad hoc auto-catalytic scheme of reaction coupled with realistic growth-kinetics (L'Heureux and Fowler,1996; Ortoleva 1990), and changes in the activity of the various species in the fluid, as a consequence of rapid changes in the fluid oxidation state (Yardley et al., 1991). The oscillatory zoning in Co-, As-bearing pyrites of the Rakha deposit of SSZ indicates episodic fluctuation of the As and Co activity ratios of the ore fluid (Chowdhury and Lentz, 2017). Such changes in fluid character typify fluid mixing systems subject to fluctuating fluid source within an active hydrothermal system (*cf*. Warren, 2016). The oscillatory pattern of Co and As observed only in Surda Pyrite IB, may be a local function of As and Co activity ratio due to rapid changes in the redox state of ore is attributed to such oscillatory zoning.

5.2.2. *Selenium, gold and associated elements in pyrite*

5.2.2.1. Selenium in Pyrite: A high portion of Se analyses of all Pyrite types- I, II, and III in EPMA (Table 2) are below the detection limits of this study, which prevents a meaningful interpretation of their distribution in all pyrite types, except Pyrite I (both IA and IB), which has detailed LA-ICP-MS data (Table 3). Selenium is able to substitute for S in the pyrite lattice, resulting in the formation of SeS^{2-} and Se^{2-} dianions. According to Abraitis et al. (2004), Se-rich pyrite is generally associated with Cu-rich deposits. In both Pyrite IA and Pyrite IB, variations in the concentrations of Se and Co in pyrite are likely controlled by the temperature (e.g., Maslennikov et al., 2009), with the higher temperature Cu-rich ores are commonly enriched in Co and Se (e.g., Hannington et al., 1999a, b).

Numerous studies have shown that Co and Se are strongly partitioned into pyrite at temperatures higher than 300 °C, and at moderately to strongly reduced conditions (e.g., Grant et al., 2018; Huston et al., 1995; Keith et al., 2017; Maslennikov et al., 2017; Revan et al., 2014). According to Keith et al. (2018), Se concentrations in pyrite vary systematically in response to changes in fluid temperature, irrespective of pH and fO_2, and thus Se contents of pyrite can be used as a geo-thermometer for the hydrothermal ore deposits.

Reduced Se species dominate all hydrothermal fluids, even oxidized sulfate-rich fluids. The concentration of Se in pyrite increases exponentially once the sulfate-dominant field is reached. If the fluid evolves to more reduced conditions, the Se content of pyrite will decrease until H_2S field is

reached and then level off (Huston et al., 1995). Variation in the Se content of pyrite could be caused by four mechanisms: (1) fractionation of Se with temperature (e.g., Bethke and Barton, 1971), (2) preferential uptake of either Se or S during sulfide precipitation to change the fluid Se/S ratio, (3) fractionation of Se owing to change in redox and/or pH conditions (Tischendorf and Ungethum, 1964; Yamamoto, 1976), or (4) mixing of hydrothermal fluids with seawater (Huston et al., 1995). There are no systematic Se variations with As, and no obvious relationship to specific mechanisms of mineral precipitation. Hence, Se can be used as a proxy to estimate the precipitation temperature of pyrite in different ore deposits.

Both Se and As occupy the S site in As^{1-} pyrite, but in the LA-ICP-MS mapping of both IA and IB type of Surda Pyrite I, no correlation is observed between Se and As in pyrites, suggesting an As-independent incorporation of Se into pyrite. In both Pyrite IA and Pyrite IB, Se and Ni are positively correlated (Figs. 8, 9, and Appendix C), and tends to increase from core to rim, though Ni occupies the Fe site in pyrite. This suggests that correlations between trace elements in pyrite may reflect external factors (and not always crystallographic factors), such as relations between elements in the source region from which they were derived (wall rocks, magmas), a similar response to depositional processes, or existence of soluble complex ions involving the two elements (Kesler et al., 2007).

5.2.2.2. Gold and associated elements in pyrite: LA-ICP-MS Au data are available in Pyrite I only. The co-occurrence of Au–Ag (Fig. 8) in both Pyrite IA and IB along pyrite fractures and grain boundaries may be indicative of the presence of electrum inclusions. A minor generation of Au are also finely dispersed in both Pyrite IA and IB without co-enrichment of Ag (Figs. 8, 10) in electrum-inclusion free areas, and is referred to as "invisible" gold (*cf.* Myagkaya et al., 2016).

Incorporation of invisible gold in pyrite can occur either via inclusion of nano-scale particles, such as native Au, tellurides, and antimonides, or incorporation of Au in the mineral structure (*cf.* Agangi et al., 2015). Gold does not show any correlation with As in the Surda Pyrite I. It has been observed that disseminated Au particles are along intragranular microfractures rather than grain boundaries (Fig. 10). Such features indicate a strain-induced deformation superimposed onto precursor pyrite in which a primary Co-As-Ni-zonation is preserved (*cf.* Ciobanu et al., 2012). These characteristics can be associated with crack healing following hydraulic brecciation via devolatilization, resulting in closure of short-lived porosity within a single crystal (Brantley et al., 1990). In the present study it is shown that this process allows for preservation of pore-attached invisible gold particles within single grains of highly strained pyrite. Enrichment of Au is also visible along cracks of Pyrite IB (Fig. 11) along with Cu, Mn, Ni, Hg, Ag, Pb, Sb, Zn, Ce, Y, U, and Th, which transgress the zoning pattern defined by As, Co, and perhaps Ni. This implies that this Au association is perhaps not intrinsic, and became enriched during later processes that are younger than As, Co, and Ni.

Enrichment of Cu, Mn, Ni, Hg, Pb, Sb, Zn, Ce, Y, U, and Th along one set of cracks, and Bi and Te along another set of cracks of Pyrite IB implying that these are perhaps not intrinsic, and were

enriched during later processes. These cracks transgress the zoning pattern defined by As, Co, and perhaps Ni indicating earlier formation of these zoned Co, As, and Ni. The relative timing between Bi-Te with Ag-Cu-Ni-Pb-Hg is unclear. The common occurrence of Bi only along the rim portion of Pyrite IB (Fig. 9) indicates a later origin for this element. According to Grundler et al. (2013), neutral to alkaline fluids can effectively mobilize and transport Te from the source region to the site of metal deposition. The incorporation of Te in pyrite is highly sensitive to redox changes in the parental fluids, and high Te contents in pyrite are related to low fO_2 of the fluid (Keith et al., 2018). The positive correlation of Bi and Te could indicate the coprecipitation of Bi tellurides and pyrite (e.g., Maslennikov et al., 2009). The microscopic inclusions of Bi telluride are also observed in the pyrite grains (Fig. 6A). Copper, Hg, V, and Zn occur both in Pyrite IA and Pyrite IB (Fig. 9). The maximum concentrations of Zn (1073 ppm) in Pyrite IB seem to indicate the presence of Zn-bearing mineral inclusions.

5.3. Nickel Pyrite (Bravoite) and Nickel-bearing Pyrite

The mode of occurrence of Ni-pyrite and associated pyrite with moderate Ni, and other mineralogical and textural evidence indicate that the hypogene Fe-Cu-Ni-rich assemblage was subjected to supergene alteration process. The restricted occurrence of these Ni-bearing pyrite, Ni-pyrite and violarite in near surface mining levels (up to 5th level; < 250 m from the surface), and their absence in deeper levels further lends support to a supergene origin for the Ni-pyrite and Ni-bearing pyrite. The secondary supergene violarite occurs along late fractures and grain margins of primary pentlandite (Fig. 4F) indicating replacement origin (*cf.* Butt and Nickel, 1981). Identical replacement textures are documented from the supergene zones of both massive and disseminated nickel deposits worldwide (e.g. Misra and Fleet, 1974; Nickel et al., 1974; Watmuff, 1974). The low analytical totals (~ 96% Table 1) combined with the mottled appearance of violarite in reflected light are consistent with Vaughan and Craig's (1985) observation that supergene violarite is often extremely porous. Microfractures in coarser violarite aggregates are developed as a result of the volume reduction associated with the replacement process (*cf.* Misra and Fleet, 1974; Nickel, 1973). As a result of the supergene alteration of pyrrhotite-pentlandite ore, pentlandite is progressively replaced by violarite, accompanied by the release of Fe and Ni. This Ni reacts with the pyrrhotite, converting some of it to a second type of violarite. When the pentlandite has been completely replaced, the pyrrhotite is dissolved and the Fe and S, together with some Ni, and sulfide species derived from the oxide zone, are re-deposited as Ni-rich pyrite (Nickel et al., 1974). When these supergene Ni-rich pyrites are re-deposited on earlier hypogene pretectonic pyrites, Ni concentration is higher towards the rim of Pyrite II located close to the Ni-rich phases. The Co distribution in the supergene violarite and coexisting Co-rich pentlandite is more or less same (Table 2). According to Misra and Fleet (1974), the Co content of supergene violarite is inherited from the precursor pentlandite in the low-temperature replacement

20

process. Relict pentlandite in the supergene zone is chemically indistinguishable from primary pentlandite, and shows variation in Ni content depending on the primary assemblage. In the case of primary pentlandite- pyrrhotite or pentlandite- only assemblages, as in the case of Surda deposit, the Ni content of pentlandite is typically 26-34 wt% (Table 2).

5.4. Implications of trace and major-element compositions of Surda chalcopyrite and its relationship with co-existing pyrite

LA-ICP-MS mapping reveals homogeneously distributed concentration of Cu in Chalcopyrite I (Figs. 13, 14). Consistent Se and Zn concentrations are noted in Chalcopyrite I and II, though a thin layer of high concentration of Se and Zn occur along rim of Chalcopyrite II (Fig. 13). Such variation of Se and Zn values may indicate the presence of grainscale compositional zoning in Chalcopyrite II. In both Pyrite IA (Fig. 9) and Pyrite IB (Fig. 8) Se are consistent with stoichiometric lattice substitution of these elements (Huston et al., 1995), while Cu and Zn occur along fractures indicating precipitation of Se during the formation of Pyrite IA. Copper (Cu) and Zn started to precipitate after the formation of Pyrite IB, and continued to precipitate during the formation of Chalcopyrite II. Bismuth and Ag occur towards grain boundary and in the lattice of Chalcopyrite II in significant levels, and along fractures and as disseminations in Chalcopyrite I (Figs. 13, 14) indicating their incorporation after Fe-Cu-Zn-Se. According to Cabri et al. (1985) and Harris et al. (1984) chalcopyrite has been demonstrated to be an excellent host for Ag in solid solution. Cobalt and Ni with traces of Zn, Hg, Pb, Mn, Sb, Bi, and Te are present as disseminated inclusions within Chalcopyrite I, and Co, Ni, Hg, Bi, Mn, Au, Sb, V and Pb occur as solid solution in Chalcopyrite II. Copper and Zn along with Bi, Te, Mn, Ni, Hg, Pb, Sb, Ag, and Au occur along cracks in both Pyrite IA and Pyrite IB indicating their precipitation during the formation of Chalcopyrite II, while invisible gold precipitated during the formation of Pyrite I. Lead, Ag, Hg, Bi, Te and Sb redistribution by remobilization from the sulfide lattice of Chalcopyrite II, and reconcentration (as inclusions of galena, electrum, bismuthinite, tellurium) within the parent mineral and Chalcopyrite I, is recognized as an important process. Such remobilization may be evolved during a sequence of fluid inputs and prolonged fluid infiltration at temperatures consistent with greenschist facies metamorphism or above, generally under oriented strain (*cf*. Larocque et al., 1995).

The high levels of Se in both Chalcopyrite I (upto 306 ppm) and Chalcopyrite II (upto 582 ppm), and Mo (upto 246763 ppm) in Chalcopyrite II indicate their precipitatation from a high-temperature hydrothermal fluid (e.g., Halbach et al., 2003; Hannington et al., 1991a; Maslennikov et al., 2009; Wang et al., 2017). According to Fouquet et al. (2010), the primary factor that controls the Se enrichment in chalcopyrite is its temperature-controlled mobility in fluids, not the source rock. However, high Mo concentrations are not observed in the Chalcopyrite I, though microscopic inclusions of molybdenite are present within Chalcopyrite I (Fig. 4G).

21

Experiments in the Cu-Fe-Zn-S system have revealed that chalcopyrite may dissolve up to 0.9 at. % Zn at 500^0C, 0.8 at.% at 400^0C, and 0.6 at.% at 300^0C (Kojima and Sugaki, 1985). According to Huston et al. (1995), concentrations up to 2,000 ppm probably reflect Zn in solid solution (substituted for Fe), but that concentrations exceeding 2,000 ppm Zn are likely the result of micro-inclusions of sphalerite. Moggi-Cecchi et al. (2002) also concluded that high Zn distributions in chalcopyrite from Italian and Slovak deposits are predominantly related to micro-scale inclusions of Zn-bearing phases. Nevertheless, high Zn values of 1.86 wt.%, 1.83 wt.%, 1.73 wt.% and 1.64 wt.% have been measured in chalcopyrite by Shalaby et al. (2004), Helmy et al. (2014), Serranti et al. (2002), and Wang et al. (2015a) respectively, and have not been attributed, in any case, to sphalerite inclusions. Higher Zn concentrations in Surda chalcopyrite are associated with higher Cd concentrations. George et al. (2018) suggested that temperature, sulfur activity, and pH are significant factors influencing $Cd/Zn_{cp.}$of chalcopyrite. The Cd: Zn ratio in chalcopyrite at Surda shows some evidence of a narrow variation (avg. 0.002 in Chalcopyrite I to avg. 0.003 in Chalcopyrite II) across the dataset. The more or less same Cd: Zn ratio in Surda chalcopyrite may be an indication of constant physiochemical conditions during crystallization (*cf*. George et al., 2018).

Lead concentrations in Chalcopyrite I at Surda are uncommonly reported in the thousands of ppm (4396 ppm), though such high concentrations are likely the result of micro-inclusions of Pb bearing phases, frequently galena. Among such anomalous reports are 7,054 ppm Pb in chalcopyrite from Yaman-Kasy, Russia (Maslennikov et al., 2009), and 0.34 wt.% Pb in chalcopyrite from the Xiaozhen Cu deposit, Shaanxi Province, China (Wang et al., 2015a). Maximum reported Pb concentrations in chalcopyrite are ordinarily in the hundreds of ppm (e.g., Bajwah et al., 1987; Moggi-Cecchi et al., 2002).

5.5. Evidence from S isotope ratios and source of sulfur

Petrological and mineralogical analyses suggest that sulfides in the Surda deposit formed at multiple stages during the evolution of the shear zone. The bulk of sulfide mineralization took place during the early stage of deformation and metamorphism. The δ^{34}S values of different generations of pyrite and chalcopyrite are indistinguishable from each other (δ^{34}S values vary from +3.9 to +6.2‰ in Pyrite I, Pyrite II, and in Chalcopyrite I, Chalcopyrite II). This might suggest - i) recycling of S derived from a similar source during the evolution of the sulfide deposit, or ii) homogenization of primary heterogeneity during superimposed pervasive hydrothermal/metamorphic event (Bekker et al., 2009) presumably under high fluid:rock ratio. As discussed previously, NanoSIMS analyses of Surda pyrite grains show heterogeneous δ^{34}S indicating small intra-grain variations in δ^{34}S values at the submillimeter scale (Fig. 15A-C) suggesting limited length scales of equilibrium. At Surda, primary pyrite growth textures are widespread, and unaffected by the limited metamorphic recrystallization. Metamorphic recrystallization appears not to have caused homogenization of Co growth zoning, so δ^{34}S

values are likely to reflect those inherited during original growth. The limited metamorphic modification of preexisting S isotope heterogeneities is to be expected if the solubility of S in the metamorphic fluids is low, or if fluids are only sparingly present. In either case, S would be mobilized on very limited length scales, and $\delta^{34}S$ values would be controlled by the isotopic compositions of the protoliths on these length scales and by crystal fractionation factors of fluids. Thus, the heterogeneities inherited from the protolith may not be strongly modified by the recrystallization process if S isotope equilibration is limited to length scales of 10–100s of microns (Giacometti et al., 2014).

In contrast to the heterogeneous $\delta^{34}S$ observed in pyrite, $\delta^{34}S$ in chalcopyrite is homogeneous, within error, at the mm scale in any sample (Fig. 15C and D). This observation can be explained by different responses of pyrite and chalcopyrite to deformation during metamorphism. Pyrite is generally brittle during deformation to temperatures above 400^0 C (Barrie et al., 2011), whereas chalcopyrite dynamically recrystallizes at temperatures as low as 300^0 C (Cox, 1987), depending on the differential stress regime and strain rate. Pyrite is consequently sluggish to reequilibrate and tends to preserve original textural and isotopic features more faithfully than chalcopyrite (*cf.* Bachinski, 1977).

Thus, from the above discussion, it becomes clear that $\delta^{34}S$ values of pyrite indicate the original source of sulfur, while $\delta^{34}S$ values of chalcopyrite is modified during metamorphism. But overall more or less same $\delta^{34}S$ values in different compositional types of pyrites and chalcopyrite from Surda deposit might indicate derivation of S from a similar source.

A narrow range of consistently positive $\delta^{34}S$ compositions (+3.9 to +6.2‰) of Surda pyrite and chalcopyrite are not typical of microbial sulfate reduction (Canfield and Raiswell, 1999). Such values are common in mantle-derived sulfur, but the ranges of $\delta^{34}S$ is typically narrower and between 0 ± 1‰ (Eldridge et al., 1991), though can reach 0 ± 3‰ (Ohmoto et al., 1986), and even +5‰ (Chaussidon and Lorand, 1990). Consistent positive (not a single data has a negative value) $\delta^{34}S$ values (heavier than typical basaltic $\delta^{34}S$ values) suggest that hydrothermal reduction of sulfate either dissolved in circulating seawater or derived from sulfate minerals might have been important for the production of isotopically heavy pyrites. During mineralization, the oxygen fugacity at the depositional sight might be presumably low, that reduced sulfur species to sulfides (H_2S, HS^-) promoting the precipitation of pyrite (Druppel et al., 2006). By laboratory experiment Kiyosu (1980) showed that, during reduction of sulfate to sulfide by reaction with dextrose at 250° to 300°C, a temperature-independent kinetic isotope fractionation of 7 to 9‰ is produced. For Surda sulfide deposit, some inorganic sulfate reduction processes at the depositional site might have produced hydrothermal sulfides with isotopic values of 4 to 6‰ in the reported temperature range (250° to 325°C from Mosabani Mines- Sarkar and Basu, 1986; 260° to 321°C from Mosabani Mines- Jaireth and Sarkar, 1986; 2.6 kb/ 370°C- 0.8 kb/ 263°C from Mosaboni Mines, 2.1 kb/ 270°C- 0.65 kb/ 217°C from Rakha Mines- Mishra et al., 2003) obtained by fluid inclusion studies on quartz from quartz-sulfide veins and pyrite-pyrrhotite geothermometer of sulfide mineralization in the SSZ. Although, the $\delta^{34}S$ data of the present study, and available data from

the previous studies, point towards isotopically heavy seawater/modified seawater/evaporite as the source of hydrothermal solution, the source of S in the Surda deposit cannot be assigned to a unique source, based solely on $\delta^{34}S$ values of sulfide.

The $\Delta^{33}S$ values of Surda sulfide range from −0.2 to +0.6‰. The average $\Delta^{33}S$ of all eight samples is 0.1 ± 0.2‰. In addition, the great majority of individual data points within each sample show zero MIF (Mass Independent Fractionation) within errors indicating MDF signature. The 'exceptional feature is that few data points showing positive $\Delta^{33}S$ between +0.3 and +0.6‰, while, in the same sample (U41), another data point shows a negative $\Delta^{33}S$ (-0.2‰). The presence of both negative and positive values of $\Delta^{33}S$ in the same pyrite sample is unlikely, and cannot have any reasonable geochemical explanation; more likely it reflects both analytical uncertainty and reproducibility.

The $\Delta^{33}S$ values close to zero ($\Delta^{33}S$ = +0.03‰ ± 0.04‰, Farquhar et al., 2002) in sulfide may be obtained in magmatic sulfur provided they are not contaminated by surface derived sulfur (in sediments or water) older than 2.4 Ga (Bekker, 2009; Penniston Dorland et al., 2008, 2012). Sulfur that has been a part of the anoxic atmosphere or hydrosphere younger than 2.4 Ga also has $\Delta^{33}S$ values close to zero. According to Ono et al. (2003), a combination of $\Delta^{33}S$ and $\delta^{34}S$ groups can be used to determine the source of S in pyrite prior to the great oxygenation event (GOE). A positive $\Delta^{33}S$ and $\delta^{34}S$ value reflect a conversion of volcanically sourced S to S_8 via atmospheric reactions. A near zero values of both $\Delta^{33}S$ and $\delta^{34}S$ reflect a volcanic SO_2 source, a negative $\Delta^{33}S$ and $\delta^{34}S$ value reflect a H_2SO_4 source, and a negative $\Delta^{33}S$ and positive $\delta^{34}S$ value reflect a seawater sulphate source. Near zero $\Delta^{33}S$ values and significantly positive $\delta^{34}S$ values of Surda sulfide are consistent with the results of Neumayr et al. (2008), who interpreted their S isotope data to represent the presence of a reduced fluid component in a fluid mixing model of ore formation. The present S isotope data also indicate derivation of sulfur from a near surface source, seawater for example, that formed the deposit after the GOE.

The utility of S and Se to determine the relative importance of seawater versus magmatic hydrothermal water lies in the distinct $\sum Se/\sum S$ ratios of these two fluids. The Se/S ratios aid in the identification of ore generating fluid sources, and can indicate mixing of fluids. Present day seawater has a molar $\sum Se/\sum S$ ratio of 2-10 x 10^{-8} (Brewer, 1975; Measures and Burton, 1980), whereas magmatic hydrothermal fluids are likely to have magmatic molar $\sum Se/\sum S$ ratios. The Se/S ratios of magmatic fluids are approximately 3×10^{-4} (Hattori, 1993; Huston et al., 1995; Lorand et al., 2003; Schneider, 1975). Igneous rocks have molar $\sum Se/\sum S$ ratios of 5 to 20 x 10^{-5} (Schneider, 1975; Sindeeva, 1964), with felsic rocks having higher values than mafic igneous rocks. Also, upper crustal rocks have estimated average 9 x 10^{-5} $\sum Se/\sum S$ ratios and lower crustal rocks have an estimated 4x 10^{-4} $\sum Se/\sum S$ ratio (Wedepohl, 1995). Mason (1982) summarized shale data for S and Se that yields a 2.5 x 10^{-5} $\sum Se/\sum S$ ratio. High Se/S ratios and low $\delta^{34}S$ values generally reflect magmatic fluids, typical of VHMS and epithermal deposits, whereas the opposite is true for basinal or evaporitic sources. The $\sum Se/\sum S$ ratios determined for both Pyrite I and Pyrite II from Surda deposit show 4.4 to 4.5 x10^{-4} in Pyrite IA

and IB, and 5.7 x10^{-4} in Pyrite II. Selenium in pyrite may vary due to changes in the $\sum$Se/$\sum$S ratio of the ore-forming fluids. Hence, in high temperature magmatic-hydrothermal systems the fluids are depleted in Se compared to their low temperature counter parts (*cf*. Huston et al., 1995; Keith et al., 2018). High Se concentrations (260 to 400 ppm) in Surda pyrite possibly indicates a lower temperature of the Cu–rich ores (250°-350°C- Jaireth and Sarkar, 1986; Mishra et al., 2003; Sarkar and Basu, 1986), and probably precipitation from a metalliferous fluid with a high $\sum$Se/$\sum$S ratio (10^{-4} to 10^{-3}), which is consistent with some igneous input of these elements (cf. Huston et. al., 1995).

Though Se/S ratio of both Pyrite I and Pyrite II is similar to that of magmatic fluids, multiple S isotope compositions of pyrite indicate that modified seawater, might likely involved in most sulfide mineralization. However, S and Se do not need to come from the same source, and additional data other than Se/S ratio may be required to distinguish these different sources of Se and S. Selenium values may have not necessarily been originated directly from magmas, but may be the result of leaching of this metal from adjacent mafic rocks by hydrothermal fluids.

5.5. *Genesis of sulfide mineralization*

In the Surda sulfide deposit, a) the presence of three compositionally different pyrites (more than one variety can be found in a single polished thin section), b) the presence of texturally different, yet compositionally similar pyrite (e.g., elongate, euhedral-subhedral, annealed) grains of Pyrite I, and c) preservation of compositional zoning within a single grain of pyrite collectively indicate that the minor element compositions of pyrite were not entirely modified during subsequent events (*cf*. Pal et al., 2009, 2011b). Thus the mode of occurrences and compositions of pyrite in the Surda deposit can potentially be used to trace the chemical evolution of sulfide mineralization in this deposit. The textures and trace element chemistry of associated three texturally and compositionally different chalcopyrites are used to trace whether a similar signature to pyrite is present.

Based on the textures of pyrite in this deposit and similar textures describe in previous studies, it is proposed that the sulfide veins containing Pyrite I formed prior to the end of deformation, and they are epigenetic hydrothermal in origin. Therefore, these Pyrite I-bearing veins are considered to be early-shearing (Fig. 16).

The chemical zonality of pyrites in the Surda deposit reflects the chemical evolution of ore bearing fluids that are not observed in any other mineral phases. The properties of the complex ions like Cl^-, NH_3, F^-, HS^-, SO_2^-, CO_2^{2-} and OH-complexes are important in determining the position of a metal in ore zoning sequence (Susak and Crerar, 1982, 1985). The thermodynamic and molecular properties of metal ion complexes are strongly influenced by temperature, pressure, and the ligand type and concentration, especially for Cu, Co, and Ni that are much more soluble with very hypersaline ore-forming systems (Susak and Crerar, 1985).

Cobalt-rich but As-free or As-poor with some Ni in Pyrite IA indicates relatively high activity of Co and S, and relatively low activity of As, Ni, and Fe during crystallization of the older pyrite generation (Pyrite IA). Some Pyrite I grains (Pyrite IA) are homogeneous in composition. Recrystallization under regional metamorphism may homogenize pyrites. However, the compositional zoning defined by variation in Co and As contents seen in Pyrite I (mainly in Pyrite IB, and some Pyrite IA) is unlikely to occur in pyrite of metamorphic origin (*cf*. Bogush, 1983; Pal et al., 2009), because fluctuating fluid parameters are not expected from a regional metamorphic fluid, which evolved in equilibrium with the surrounding host lithologies. So compositional zoning also support that Pyrite I most likely formed during the early stages of the evolution of the Singhbhum Shear Zone. Thus, lack of chemical zoning observed in some of the samples of Pyrite 1A suggests that Co-rich mineralizing fluid had a relatively homogeneous chemical composition during the growth of this pyrite in places. The compositional homogeneity in such homogeneous Pyrite IA and in individual zones of zoned Pyrite 1A (evident from element distribution maps) also suggests that Co and Ni were incorporated in pyrite through solid solution substituting Fe, and not as submicroscopic mineral inclusions. Growth zoning is common in hydrothermally deposited pyrites (e.g. Ramdohr, 1969), and may reflect fluctuations in temperature, pH, or precipitation of pyrite from an aqueous solution under conditions of varying Co/Ni activity. Elongated Pyrite IB grains of Surda are interpreted to be related to hydrothermal mineralization predating ductile deformation (*cf*. Pal et al., 2009). The patchy zoning of Co present in Pyrite IA may be due to dissolution-re-precipitation (DRP reaction-replacement) during the chemical evolution of this pyrite (*cf*. Agangi et al., 2015). Overgrowth of As-rich Pyrite IB with Co (lower than Pyrite IA) on Pyrite IA implies sudden changes in the fluid chemistry (and temperature?), coupled with a sharp increase in As activity, and decrease in the Co activity. Nickel shows slight increase in this later fluid, still it has a very low concentration compared to Pyrite II. Chalcopyrite I (Ni-content higher than that of Pyrite IB) precipitated from this fluid after the formation of Pyrite IB. The lack of As in Pyrite II, which in some cases occurs as overgrowths on As- rich Pyrite IB, gives an indication of an increase in As concentration in the fluid from early stage as the mineralization progressed. The paragenetic sequence further suggests that Co activities attained maximum values during the formation of Pyrite IA, and As activities attained maximum values during the formation of Pyrite IB. Arsenic occurred in the fluid in a very short period, while Co content decrease gradually from Pyrite IA to Pyrite IB. The second stage of pyrite deposition (Pyrite II) refers to Ni-rich pyrite, not only forming overgrowths on Pyrite I in some localities, but also occurs as subhedral grains in association with other sulphides and silicates. Replacement and fracture filling of Pyrite I by Pyrite II in the concordant Fe-Cu sulfide vein indicate that the fluid composition changed from Co-rich to Ni-rich, and Ni-activity markedly increased in the later fluid. The association of Pyrite II with other Ni-rich sulphide phases, like Ni-rich pyrrhotite and violarite, also indicates that precipitation occurred from a Ni-rich fluid and low sulphur activity. Confirmation of this proposition is further derived from replacement of Pyrite I by Ni-sulfide minerals,

26

and corresponding compositional modification of Pyrite I to Pyrite II close to the zone of replacement. It has been proposed that Ni concentration of this later fluid might have been so high in places that it led to the simultaneous crystallization of Ni-phases (pentlandite), as well as resulted in Ni-enrichment of existing pyrite and perhaps precipitation of Ni (+ Co) rich pyrite (Pyrite II). Textural features suggest that Ni-rich Chalcopyrite II started to crystallize along with Pyrite II from the later Ni-rich fluid, and continued to precipitate after the formation of Pyrite II. The similar distribution of Ni and Co in both Chalcopyrite I and II (evidenced from LA-ICP-MS maps) indicate that Co and Ni precipitated simultaneously during chalcopyrite growth. The replacement of corroded Pyrite II by Chalcopyrite II (Fig.4B) indicates precipitation of abundant Ni-rich pyrite during the late stage may had provoked a decrease of the temperature and pH of the hydrothermal fluid, inducing the observed dissolution of some early Fe-Cu sulfides, and their re-precipitation. This event of hydrothermal fluid evolution can be further extended to a less Ni-rich fluid that was incapable of precipitating Ni-bearing phases and incorporated Ni as trace elements alone in pyrite, making its concentration very high, and forms Ni-rich rims in Pyrite II. Although the Fe + Cu + Co and Fe + Cu + Ni sulfide veins are parallel to the pervasive foliation, the mutual relations amongst these veins are not very conclusive. However, the overgrowth of Ni-rich Pyrite II on Co-rich Pyrite I (Fig.4B) indicates that Pyrite II grew at a later stage after the formation of Pyrite I (*cf.* Pal et al., 2011b). Pyrite II is interpreted to be premetamorphic due to the lack of inclusion of surrounding sulphide phases and the presence of growth zoning defined by variation in Ni content. The foliation parallel veins with Pyrite II and the fragmented nature of Pyrite II further implies that Ni-sulfide veins also formed at some point prior to the end of deformation. So this is also early-shearing, but younger than Pyrite I (Fig.16). Some Ni-bearing composite pyrites occurring along with Ni-pyrite, violarite, pentlandite, and pyrrhotite in veinlets within Chalcopyrite I of Fe + Cu + Ni sulfide veins indicate their formation postdated Pyrite II (Fig.16).

The final stage of fluid evolution is represented by distinctly euhedral grains of Pyrite III (Fig. 4J). The depletion of trace elements and lack of chemical zoning observed in Pyrite III suggests that the mineralizing fluid is depleted in trace elements, and had a relatively homogenous chemical composition. Alternatively, it can be suggested that Pyrite III crystallization may be related to a metamorphic fluid, which evolved in equilibrium with the host lithologies as the fluid would not be expected to vary in its chemical composition. Overgrowth of Pyrite III on Pyrite I suggests that
Pyrite III formation postdated that of Pyrite I (Fig.4J). The re-crystallized nature of both Pyrite II and Pyrite III (Fig. 4E and L) further indicates their formation prior to the cessation of metamorphism. Minor inclusion-free chalcopyrites (Chalcoyrite III) are cogenetic with Pyrite III.

In the absence of any distinctive textural relations between Pyrite II and Pyrite III, Chalcopyrite II and Pyrite III, and Chalcopyrite II and Chalcopyrite III, we cannot place the relative timing of these compositional types (Fig. 16). Pyrite is ubiquitous at all temperatures, but chalcopyrite is generally associated with moderate to high temperature deposits. The depositional temperatures found for Cu-

rich deposits tend to occur dominantly between 200° and 350°C, while substantial Fe may continue to precipitate at even lower temperatures (Crear and Barnes, 1976). In the Singhbhum Cu-U belt cooling of hydrothermal solutions from temperatures between 260°C and 350°C was the dominant factor that caused ore deposition (Jaireth and Sarkar, 1986). Though the general cause of the deposition of pyrite is decreasing temperature, but because sulfides occur on virtually every fracture in the ore zone, reaction of the solution with the rock, perhaps causing an increase in pH, is probably the local cause for precipitation.

It is generally considered that Co and Ni are commonly associated with fluids derived from a mafic magma or have been leached by fluid from a mafic source rock containing these elements (Clark et al., 2004; Goldschmidt, 1954; Ingham et al., 2014). As Ni is easily incorporated into the pyrite crystal lattice, and is not released during hydrothermal pyrite recrystallization, Ni distribution patterns may provide information on the environment of pyrite formation (Koglin et al., 2010; Large et al., 2009). The south of the Singhbhum Cu-U belt is dominated by mafic-ultramafic volcanic and volcaniclastic rocks of Dhanjori Group enriched in Ni and Co, which may be the source of these elements forming Surda sulfide deposit.

Many studies of trace elements have related the Co/Ni ratio in pyrite to ore deposit type (Bajwah et al., 1987; Bralia et al., 1979; Koglin et al., 2010; Large et al., 2009; Loftus-Hills and Solomon, 1967; Meyer et al., 1990). Volcanogenic pyrite without accompanying Pb- and Zn-bearing minerals shows high Co and Ni concentrations with Co/Ni values greater than 1 (Bralia et al., 1979; Loftus-Hills and Solomon, 1967). High Co/Ni ratios occur in pyrite from volcanogenic ores (~ Co/Ni >10), whereas lower temperature hydrothermal pyrite generally has Co/Ni ratios between ~10 and 5 (Bralia et al., 1979). Pyrite with highly variable Co/Ni ratios, typically greater than 1, is considered to be of hydrothermal origin (Bralia et al., 1979; Cook, 1996). The compositional variations in different pyrite types based on Co and Ni had been observed by earlier workers on other sulfide deposits in the SSZ are plotted in Fig. 5B (Chowdhury and Lentz, 2017; Pal et al., 2011; Pal et al., 2009; Sarkar and Basu, 1986), which show similarity with this data.

Pyrite from orthomagmatic segregation deposits displays high, but variable, Co and Ni contents (up to wt% levels), and generally Co/Ni ratios of < 1 (e.g. Campbell and Ethier, 1984; Piña et al., 2013). Reich et al. (2016) plotted Co- and Ni-rich pyrite from magmatic Cu-Ni, VMS, porphyry Cu-Mo, Fe-Cu skarn, orogenic Au, and IOCG deposits in a Co vs. Ni diagram. It has been observed that Co and Ni analyses of pyrite from the Ernest Henry and the Manto Verde IOCG deposit (Chile) show a spread of Co/Ni ratios that vary from less than 0.5 to > 2. The few pyrite data reported for the Manto Verde IOCG deposit (Chile) show characteristically high Co/Ni ratios (> 2). The spread of Co/Ni ratios observed in the Surda pyrite (0.05 to > 2) of the present study is in agreement with data available for pyrite from IOCG deposits (Fig. 5B). Although trace element compositions of pyrite alone cannot help deciphering the deposit type, the geochemical characters of Surda pyrites and the metal association are somewhat

similar to iron oxide (–Cu–U–REE) type deposits in the world (*cf*. Pal et al., 2009, 2010, 2011a, b), although more elaborate study is needed. Previous studies in the SSZ indicated the involvement of high salinity fluid associated with U and sulfide mineralization, and alteration (Changkakoti et al., 1987; Mishra et al. 2003; Nayak and Panchapakesan, 1990; Pal et al., 2008; Pal and Bhowmick, 2015). From fluid inclusion studies and stable isotope results from Mosaboni mines in the SSZ, Jaireth and Sarkar (1986) and Changkakoti et al. (1986) suggested that the copper deposits of SSZ originated from dense, saline chloride-rich hydrothermal solution, which had a meteoric precursor or from deeply circulating meteoric waters. High-temperature laboratory experiments (Burnham, 1979; Candela and Piccoli, 1995) and fluid inclusion studies (Heinrich, 2005; Rankin et al., 1992; Wilson et al., 1980) show that the ore metals along with major salts ($NaCl$, KCl, $FeCl_2$, $MnCl_2$, and $CaCl_2$) in magmatic fluids, commonly reaching concentrations of thousands of ppm to a few wt.%. Based on boron isotope compositions of tourmaline and S isotope compositions of sulfide minerals of Jaduguda U (-Cu-Fe) deposit, SSZ, Pal et al. (2010, 2011b) suggested that a basinal brine or modified seawater was involved in the early-shearing uranium mineralization in the nearby uranium deposit. So the associated sulfide mineralization in the Surda deposit may have involved a high salinity fluid in the mineralized zones. The $\delta^{34}S$ isotope compositions obtained in the present study, in tandem with; a) widespread occurrence of alkali alteration, b) involvement of high salinity fluid in the mineralized zones, c) boron isotopic character of tourmaline (a more powerful indicator of fluid source though not necessarily sulfur source) collectively point towards seawater as the likeliest source for S in the Surda deposit.

The Pb-Pb geochronology of SSZ sulfide yielded an age of ~1.77 Ga (Johnson et al., 1993). However, as there are multiple stages of hydrothermal mobilization and mineralization, mineral separates that might bear the signature of multiple events are likely to yield erroneous or simply metamorphic (e.g., reset) Pb-Pb ages. Moreover, our study has shown that micro-crystalline uraninite inclusions occur in pyrite, which can thus yield erroneous ages in the U-Th-Pb geochronological approaches for sulfides. *In situ* dating of allanite from a deposit in the SSZ yielded multiple events of fluid flux at ~1.88 Ga, ~1.66 Ga, and at 1.0 Ga (Pal et al., 2011a) in the shear zone; the 1.66 Ga is assigned to deformation and metamorphism in the shear zone (Fig. 16). Similar events of hydrothermal fluid flux associated with U mineralization have also been demonstrated from using geochemistry and chemical dating of uraninite (Pal and Rhede, 2013). In light of the above discussion we propose that the Surda sulfide deposit formed in Paleoproterozoic (~1.8-1.9 Ga) by hydrothermal process involving seawater/modified seawater/evaporites after 2.4 Ga, which explains a predominant MDF signature of the sulfide minerals and also consistent positive $\delta^{34}S$ values.

6. Concluding remarks

1. The study presents new major and trace element data, and multiple sulfur isotope geochemistries for pyrite and chalcopyrite of the Surda sulfide deposit in the context of ore textures. Based on mode of occurrence, texture and mineralogical association, pyrite and chalcopyrite are classified into three types. Pyrite I (Pyrite IA + Pyrite IB) + Chalcopyrite I in magnetite + apatite bearing pyrite I + chalcopyrite I + pyrrhotite veins; Pyrite II + Chalcopyrite II in pentlandite, Ni-pyrite bearing pyrite II + pyrrhotite + chalcopyrite II ± violarite veins, and Pyrite III + Chalcopyrite III as disseminated grains. Textural relationship indicates that Pyrite IA is earliest pyrite generation. Pyrite IB formation predates Pyrite II, Pyrite III, and Chalcopyrite I. Chalcopyrite II is cogenetic with Pyrite II, and continued to precipitate after the formation of Pyrite II. Chalcopyrite III started to crystallize along with Pyrite III. All pyrite and chalcopyrite types are early-shearing, formed prior to the closing of deformation and metamorphism. Though Pyrite II of hypogene origin is early-shearing, some Ni-bearing pyrites along with Ni-pyrite and violarite were formed by supergene alteration processes, and post tectonic.

2. The major- and trace-element compositions of various pyrite and chalcopyrite grains were constrained by BSE imaging coupled with EPMA and LA–ICP-MS analysis. Three compositional types (I, II, and III) of both pyrite (based on the concentrations of Co and Ni) and chalcopyrite (based on minor elements) have been identified. Pyrite I is further subdivided into Pyrite IA and IB based on their As content. Pyrite I shows notable concentrations of high temperature fluid-mobile elements. Pyrite IA is enriched in Co (up to 5.5 wt.%), while Pyrite IB is enriched in As (up to 2.6 wt.%) and Co (up to 4.7 wt.%), with complementary enrichments in Sb, Bi, Cu, Mn, Ni, Pb, V, Se, and Ag. Gold occurs in Pyrite IB as minor "invisible" gold, along with Ag as electrum inclusions along pyrite fractures and grain boundaries, and also along cracks of Pyrite IB along with Cu, Mn, Ni, Hg, Ag, Pb, Sb, Zn, Ce, Y, U, and Th, which transgress the zoning pattern defined by As, Co, and perhaps Ni. Pyrite II is enriched in Ni (up to 3.8 wt.%). Chalcoyrite I shows homogeneous distribution of Fe, Cu, Zn, and Se, whereas the pattern for Co, Ni, Hg, Bi, Mn, Ag, Sb, V and Pb show increase of concentrations towards rim of Chalcopyrite II. Both Pyrite III and Chalcopyrite III are Co-, Ni-poor. Selenium precipitated during the formation of Pyrite IA, and continued to precipitate during the formation of Pyrite III. Copper and Zn precipitated after formation of Pyrite IB, and continued to precipitate during formation of Chalcopyrite I. Bismuth, Mn, Au, Sb, and Pb precipitated during the formation of Chalcopyrite II, while invisible (refractory) gold precipitated during the formation of Pyrite IB.

3. The chemical zonality of pyrite reflects chemical changes in ore-bearing fluids that are not recorded by any other mineral phases. Cobalt and Ni contents decrease from Pyrite IA to Pyrite IB. Arsenic and Co are incorporated in Pyrite IB by a cobaltite-type $(Fe_{1-x}Co_x)(S_{1-x}As_x)_2Fe$ $(As_xS_{1-x})_2$ substitution mechanism. The decreasing of As-content of Pyrite IB in an oscillatory manner from the core to the rim, similar to that of Co may reflect changes in the activity of As, Co, and (or) in

the *P-T* conditions, and also may indicate that the chemical ambience during the formation of Pyrite 1B was likely more reducing. The rapid changes in the redox states in ore fluid caused fluctuation of the As and Co activity affecting the As/Co ratio, and subsequent oscillatory zoning of As and Co in Co-As-rich pyrites.

4. Based on the depositional environment and multiple S isotope compositions of pyrite and chalcopyrite, it can be suggested that the source of S that involved in sulfide mineralization, might be seawater sulfate or modified seawater (brine/evaporite etc.).

5. The MDF signatures measured in the Surda sulfide deposit point to the mineralization event that took place after the great oxidation event

Acknowledgements

References

Abraitis, P.K., Pattrick, R.A.D., Vaughan, D.J., 2004. Variations in the compositional, textural and electrical properties of natural pyrite: a review. - Int. J. Miner. Process. 74, 41–59.

Acharyya, S.K., Gupta, A., Orihashi, Y., 2010a. New U-Pb zircon ages from Paleo-MesoarcheanTTG gneisses of the Singhbhum Craton, Eastern India. Geochem. J. 44, 81- 88.

Agangi. A., Przybylowicz, W., Hofmann, A., 2015. Trace element mapping of pyrite from Archean gold deposits – A comparison between PIXE and EPMA. Nuclear Instruments and Methods in Physics Research B 348, 302–306.

Atkinson, B.K., 1975. Expreimental deformation of polycryatalline pyrite: Effects of temperature, confining pressure, strain rate and porosity. Econ. Geol. 70, 473-487.

Bachinski, D. J., 1977. Sulfur isotopic composition of ophiolitic cupriferous iron sulfide deposits, Notre Dame Bay, Newfoundland. Econ. Geol., 72, 243–257, doi:10.2113/gsecongeo.72.2.243.

Bajwah, Z.U., Secombe, P.K., Offler, R., 1987. Trace element distribution, Co:Ni ratios and genesis of the Big Cadia iron-ore deposit, New South Wales, Australia. Mineral. Deposita 22, 292–300.

Ball, V., 1870. On the Copper of Dhalbhum and Singhbhum. Record Geol. Surv. Ind., 3, 95 p.

Ballantyne, J.M., Moore, J.N., 1988. Arsenic geochemistry in geothermal systems. Geochem. Cosmochim. Acta 52, 475-483.

Banerji, A.K., 1962. Cross-folding, migmatization and ore localisation along parts of the Singhbhum shear zone, south of Tatanagar, Bihar, India. Econ. Geol. 57, 50–71.

Barrie, C.D., Pearce, M.A, Boyle, A.P., 2011. Reconstructing the pyrite deformation mechanism map. Ore Geol. Rev. 39, 265–276.

Barton, P.B., 1970. Sulfide petrology. Min. Soci.Am., Sp. paper 3,187- 198.

Baublys, K.A., Golding, S.D., Young, E., Kamber, B.S., 2004. Simultaneous determination of delta (33) SV-CDT and delta S-34(V-CDT) using masses 48, 49 and 50 on a continuous flow isotope ratio mass spectrometer. Rapid Commun. Mass Spectrometer 18, 2765–2769.

Bayliss, P., 1989. Crystal chemistry and crystallography of some minerals within the pyrite group. Am. Mineral. 74, 1168-1176.

Bekker, A., Barley, M.E., Florentini, M.L., Rouxel, O.J., Rumble, D., Beresford, SW, 2009. Atmospheric sulfur in Archean komatitite-hosted nickel deposits. Science 326, 1086-1089.

Bethke, P.M., Barton, P.B, 1971. Distribution of some minor elements between coexisting sulfide minerals. Econ. Geol. 66, 140-163.

Bhattacharya, H.N., Mahapatra, S., 2008. Evolution of the Proterozoic rift margin sediments- North Singhbhum Mobile Belt, Jharkhand-Orissa, India. Precamb. Res. 162, 302- 316.

Bogush, I.A., 1983. Evaluation of productivity and mode of functioning of endogene sulphide-ore Sources on the basis of groth zoning in pyrite. Transactions (Docklady) of the USSR Academy of Sciences. Earth Sci. Sections 258, 149-154.

Bose, M.K., 2009. Precambrian mafic magmatism in the Singhbhum craton, eastern India. J. Geol. Soc. Ind. 73, 13-35.

Bralia, A., Sabatini, G., Troja, P., 1979. A reevaluation of the Co/Ni ratio in pyrite as geochemical tool in ore genesis problems. Mineral. Deposita 14, 353–374.

Brandeis, G., Jaupart, C., Allegre, C. J., 1984. Nucleation, crystal growth and the thermal regime of cooling magmas. J. Geophys. Res. 89:10161-10177.

Brantley, S.L., Evans, B., Hickman, S.H., Crerar, D.A., 1990. Healing of microcracks in quartz:

32

Implications for fluid flow. Geology, 18, 136–139.

Brewer, P.G., 1975. Minor elements in seawater: In: Riley J. P., Skirrow, G. (Eds.). Chem. Oceanography London, Academic Press, 1, 365-414.

Burnham, C.W., 1979. Magmas and hydrothermal fluids. In: Barnes, H.L. (Ed.), Geochemistry of Hydrothermal Ore Deposits. 2 ed.: New York, Wiley Inter Science, p. 71– 136.

Butt, C.R.M., Nickel, E.H., 1981. Mineralogy and geochemistry of the weathering of the disseminated nickel sulfide deposit at Mt. Keith, western Australia. Econ. Geol.76, 1736-1751.

Cabri, L.J., Campbell, J.L., Gillies Laflamme, J.H., Leich, R.G., Maxwell, J.A., Scott, J.D., 1985. Proton-microprobe analysis of trace elements in sulfides from some massive-sulfide deposits. Can. Mineral. 23, 133-148.

Candela, P.A., Piccoli, P.M., 1995. Model ore-metal partitioning from melts into vapor and vapor/brine mixtures. In: Thompson, J.F.H. (Ed.), Magmas, Fluids and Ore Deposits. Mineral. Association of Canada Short Course 23, 101–127.

Campbell, F.A, Ethier, V.G., 1984. Nickel and cobalt in pyrrhotite and pyrite from the Faro and Sullivan orebodies. Can. Mineral. 22, 503–506.

Canfield, D.E., Raiswell, R., 1999. The evolution of the sulfur cycle. Am. J. Sci. 299, 697-723.

Chatterjee, A., Banerjee, M., Bhattacharya, A., Maji, A.K., 2010. Monazite chronology, Metamorphism anatexis and tectonic relevance of the mid-Neoproterozoic Eastern Indian Tectonic Zone. Precamb. Res. 179, 99-120.

Changkakoti, A., Gray, J., Morton, R.D., Sarkar, S.N., 1987. The Mosabani Copper Deposit, India- a Preliminary study of nature and genesis of the ore fluids. Econ. Geol. 82, 1619- 1625.

Chaussidon, M., Lorand, J.P., 1990. Sulfur isotope composition of orogenic spinel lherzolite massifs from Ariège (North-eastern Pyrenees, France): an ion microprobe study. Geochem. Cosmochim. Acta 54, 2835-2846.

Chowdhury, S., Lentz, D.R., 2017. Minor- and trace- element characteristics of different pyrite types and their S- isotope geochemistry from the Proterozoic Rakha Copper deposit, Singhbhum Shear Zone, India. J. Mineral. Geochem. 194 (3), 251-277.

Ciobanu, C.L., Cook, N.J., Utsunomiya, S., Kogagwa, M., Green, L., Gilbert, S., Wade, B., 2012. Gold-telluride nanoparticles revealed in arsenic-free pyrite. Am. Miner., 97, 1515–1518.

Clark, C., Grguric, B., Mumm, A.S., 2004. Genetic implications of pyrite chemistry from the Paleoproterozoic Olary Domain and overlying Neoproterozoic Adelaidean sequences, northeastern South Australia. Ore Geol. Rev. 25, 237-257.

Cook, N.J., 1996. Minearlogy of the sulfide deposits at Sulitjelma, Northern Norway. Ore Geol. Rev. 11, 303-338.

Cook, N.J., Fanning, C.M., Ashley, P.M., 1994. New geochronological results from the Williyama Supergroup, Olary Block, South Australia. Aus. Res. Ore Gen. Symp. Aust. Mineral.

Foundation, Adelaide 19.1- 19.5.

Cook, N.J., Ciobanu, C.L., Mao, J., 2009. Textural controlon gold distribution in As-free pyrite from the Dongping, Huangtuliang and Hougou gold deposits, North China craton (Hebei Province, China). Chem. Geol. 264, 101–121.

Cox, S. F., Etheridge, M.A., Hobbs, B.E., 1981. The experimental ductile deformation of polycrystalline and single crystal pyrite. Econ. Geol. 76, 2105- 2177.

Cox, S.F., 1987. Flow mechanisms in sulfide minerals. Ore Geol. Rev. 2, 133- 171.

Craig, J.R., Vokes, F.M., 1993. The metamorphism of pyrite and pyrite ores: an overview. Mineral. Mag. 57, 3-18.

Craig, J.R., Vokes, F.M., Solberg, T.N., 1998. Pyrite: physical and chemical textures. Mineral. Deposita 34, 82-101.

Crerar, D.A., Barnes, H.L., 1976. Ore Solution Chemistry V. Solubilities of chalcopyrite and chalcocite assemblages in hydrothermal solution at 200° to 350°C. Econ. Geol. 71, 772-794.

Deditius AP, Utsunomiya S, Renock D, Ewing RC, Ramana CV, Becker U, Kesler SE , 2008. A proposed new type of arsenian pyrite; composition, nanostructure and geological significance. Geochim Cosmochim Acta 72:2919–2933.

Dehnavi, A.S., McFarlane, C.R.M., Lentz, D.R., Walker, J.A., 2018. Assessment of pyrite composition by LA-ICP-MS techniques from massive sulfide deposits of the Bathurst Mining Camp, Canada: From textural and chemical evolution to its application as a vectoring tool for the exploration of VMS deposits. Ore Geol. Rev. 92, 656-671.

Druppel, K., Wagner, T., Boyce, A.J., 2006. Evolution of sulfide mineralization in Ferro carbonatite Swartboois drif, northwestern Namibia: constraints from mineral compositions and sulfur isotopes. Can. Mineral. 44, 877-894.

Dunn, J.A., 1929.The geology of north Singhbhum including parts of Ranchi and Manbhum districts. Mem. Geol. Surv. Ind. 54, 1-166.

Dunn, J.A., 1937. Mineral deposits of eastern Singhbhum and surrounding areas. Mem. Geol. Surv. Ind. 69, 1-279.

Dunn, J.A., Dey, A.K., 1942. The geology and petrology of eastern Singhbhum and surrounding Areas. Mem. Geol. Surv. Ind. 69, 281-456.

Eames, A.G., Barker, S.L.L., Durance, P.M.J., 2016. Pyrite geochemistry and textures in the epithermal Au-Ag mineralisation at Waihi. In Geoscience Society of New Zealand. Geosciences 2016. Conference held at Lake Wanaka Centre, Wanaka, New Zealand.

Edenborn, H. M., Belzile, N., Mucci, A., Lebel, J., Silverberg, N., 1986. Observations on the diagenetic behavior of arsenic in deep coastal sediment. Bio geochem. 2, 359-376.

Eldridge, C.S., Compston, W., Williams, I.S., Harris, J.W., Bristo, J.W., 1991. Isotope evidence for the involvement of the recycled sediments in diamond formation. Nature 353, 649-653.

Farquhar, J., Wing, B.A., McKeegan, K.D., Harris, J.W., Cartigny, P., Thiemens, M.H., 2002. Mass-independent sulfur of inclusions in diamond and sulfur recycling on early earth. Science 298, 2369–2372.

Fleet, M.E., Maclean, P.J., Barbier J., 1989. Oscillatory-zoned As-bearing pyrite from strata-bound and stratiform gold deposits: An indicator of ore fluid evolution. Econ. Geol. Monograph 6, 356–362.

Fleet, M.E., Chryssoulis, S.L., Maclean, P.J., Davidson, R., Weisener, G.G., 1993. Arsenian pyrite from gold deposits—Au and As distribution investigated by SIMS and EMP, and color staining and surface oxidation by XPS and LIMS. Can. Mineral. 31, 1–17.

Fouquet, Y., Pierre, C., Etoubleau, J., Charlou, J.L., Ondréas, H., Barriga, F.J.A.S., Cherkashov, G., Semkova, T., Poroshina, I., Bohn, M., Donval, J.P., Henry, K., Murphy, P.J., Rouxel, O., 2010. Geodiversity of hydrothermal along the midatlantic ridge and ultramafic-hosted mineralization: a new type of oceanic Cu-Zn-Co-Au volcanogenic massive sulfide deposit. In: Rona, P.A., Devey, C.W., Dyment, J., Murton, B.J. (Eds.), Diversity of Hydrothermal Systems on Slow Spreading Ocean Ridges. AGU, Washington, D.C., pp. 321–367.

Franchini, M., McFarlane, C., Maydagán, L., Reich, M., Lentz, D.R., Meinert, L., Bouhier, V., 2015. Trace metals in pyrite and marcasite from the Agua Rica porphyry-high sulfidation epithermal deposit, Catamarca, Argentina: Textural features and metal zoning at the porphyry to epithermal transition. Ore Geol. Rev. 66, 366–387.

George, L.L., Cook, N.J., Crowe, B.B.P., Ciobanu, C.L., 2018. Trace elements in hydrothermal chalcopyrite. Mineral.Mag. 82, 59-88.

Ghosh, A. K., 1972.Trace element geochemistry and genesis of the copper ore deposits of the Singhbhum shear zone, Eastern India. Mineral. Deposita.7, 292-313.

Giacometti, F., Evans, K. A., Reaby, G., Cliff, J., Tomkins, A. G., Rossetti, P., Vaggelli, G., Adams, D.T, 2014. Sulfur isotope evolution in sulfide ores from Western Alps: Assessing the influence of subduction-related metamorphism. Am. Geophys. Union, Geochem., Geophys. Geosys.15, 3808–3829, doi:10.1002/2014GC005459.

Goldschmidt, V.M., 1954. Geochemistry. The Clarendon Press, Oxford, 730 p.

Grant, H.L.J., Hannington, M.D., Petersen, Frische, ., Fuchs, S.H., 2018. Constraints on the behavior of trace elements in the actively-forming TAG deposit, Mid-Atlantic Ridge, based on LA-ICP-MS analyses of pyrite. Chem. Geol. 498, 45-71.

Grundler, P.V., Brugger, J., Etschmann, B.E., Helm, L, Liu, W., Spry, P.G., Tian, Y., Testemale, D., Pring, A., 2013. Speciation of aqueous tellurium(IV) in hydrothermal solutions and vapors, and the role of oxidized tellurium species in Te transport and gold deposition. Geochim Cosmochim Acta 120, 298–325.

Halbach, P., Fouquet, Y., Herzig, P., 2003. Mineralization and compositional patternsin deep-

sea hydrothermal systems. In: Tunni cliffe, V., Hein, J.R. (Eds.), Energy and Mass Transfer in Marine Hydrothermal Systems. Dahlem University Press, Berlin, Germany, p. 85–122.

Hannington, M.D., Bleeker, W., Kjarsgaard, I., 1999a. Sulfide mineralogy, geochemistry, and ore genesis of the Kidd Creek Deposit; Part I, North,Central and South orebodies. In: Hannington, M.D., Barrie, C.T. (Eds.), The Giant Kidd Creek Volcanogenic Massive Sulfide Deposit, Western Abitibi Subprovince. Soc. Econ. Geol., Can. 163–224.

Hannington, M.D., Barrie, C.T., Bleeker, W., 1999b. The Kidd Creek Volcanogenic Massive Sulfide Deposit: Summery and Conclusions. Econ. Geol. Monograph 10, The Giant Kidd Creek Volcanogenic Massive Sulfide Deposit, Western Abitibi Subprovince, Canada, M.D. Hannington and C.T. Barrie, 661-672.

Harris, D.C., Cabri, L.J., Nobiling, R., 1984. Silver bearing chalcopyrite, a principal source of silver in the Izok lake massive-sulfide deposit: confirmation by electron and proton-microprobe analyses. Can. Mineral. 22, 493-498.

Harms, U., 2009. Nickelone pyrite from Prangenhaus quarry, Niederberg area, Germany. A short communication. Chemie der Erde 69, 279-285.

Hattori, K.H., 1993. High sulfur magma, a product of fluid discharge from underlying mafic magma. Evidence from Mount Pinatubo, Philippines. Geology 21, 1083-1086.

Hauri, E.H., Papineau, D., Wang, J., Hillion, F., 2016. High-precision analysis of multiple sulfur isotopes using NanoSIMS. Chem. Geol. 420, 148–161.

Helmy, H.M., Shalaby, I.M., Rahman, H.A., 2014.Large-scale metal zoning in a late Precambrian skarn-type mineralization: Wadi Kid, SE Sinai, Egypt. J. Afr. Ear. Sci.90, 77-86.

Heinrich, C.A., 2005. The physical and chemical evolution of low-salinity magmatic fluids at the porphyry to epithermal transition: a thermodynamic study. Mineral. Deposita 39, 864–889.

Huston, D.L., Sie, S.H., Cooke, D.R., Both, R.A., 1995. Trace elements in sulfide minerals from eastern Australian volcanic-hosted massive sulfide deposits: Part I. Proton microprobe analyses of pyrite , chalcopyrite, and sphalerite, and Part II. Selenium levels in pyrite: Comparison with $\delta34S$ values and implications for the source of sulfur in volcanogenic hydrothermal systems. Econ. Geol. 90, 1167-1196.

Ingham, E.S., Cook, N.J., Cliff, J., Ciobanu, C.L., Huddleston, A., 2014. A. Combined chemical, isotopic and microstructural studyof pyrite from roll-front uranium deposits, Lake Eyre Basin, South Australia. Geochem. Cosmochim. Acta 125, 440- 465.

Jaireth, S., Sarkar, S.N., 1986. Fluid inclusions studies in quartz from quartz-sulphide veins of Central Section, Mosaboni mines, Singhbhum Copper Belt, Bihar. Abstract *in* Geology and Geochemistry of sulfide ore bodies and associated rocks in mosaboni and Rakha Mines sections in the Singhbhum Copper Belt. A Diamond Jubilee Monograph, Sarkar, S.N. and associates, Ind. Sch. Mines, Dhanbad, 122 p..

Johnson, P.T., Dasgupta, D., Smith, A.D., 1993. Pb-Pb systematic of copper sulfide mineralization, Singhbhum area, Bihar. Ind. J. Geol. 65, 211-213.

Keith, M., Hackel, F., Hasse, K.M., Schwarz-Schampera, U., Klemd, R., 2016. Trace element systematics of pyrite from submarine hydrothermal vents. Ore Geol. Rev. 72, 728-745.

Keith, M., Smith, D,J., Jenkin, G.R.J., Holwell, D.A., 2017. Global Se and Te systematics in hydrothermal pyrite from different ore deposits: a review. Applied Ear. Sc., 126:2, 70-71, DOI: 10.1080/03717453.2017.1306265.

Keith, M., Smith, D.J., Jenkin, G.R.T., Holwell, D.A., Dye, M.D., 2018. A review of Te and Se Systematic from hydrothermal pyrite from precious deposits: Insights into ore-forming processes. Ore Geol. Rev. 96, 269-282.

Kelly, W.C., Clark, B.R., 1975. Sulfide deformation studies: 111. Experimental deformation of chalcopyrite to 2,000 bars and 500^0 C. Bull. Soc. Econ. Geol. 70, 431- 453.

Kesler, S.E., Deditius, A.P., Chryssoulis, S., 2007. Geochemistry of Se and Te in arsenian pyrite: new evidence for the role of Se and Te hydrothermal complexes in Carlin and epithermal-type deposits. In: Kojonen, K.K., Cook, N.J., and Ojala, V.J. (Eds.), Au–Ag–Te–Se deposits: Proceedings of the 2007 Field Workshop (Espoo, Finland, August 26–31, 2007), Geol. Surv. Finland 53, 85–95.

Kiyosu, Y., 1980. Chemical reduction and sulfur-isotope effects of sulfate by organic matter under hydrothermal conditions. Chem. Geol. 30, 47-56.

Koglin, N., Frimmel, H.E., Minter, W.E.L., Brätz, H., 2010. Trace-element characteristics of different pyrite types in Mesoarchaean to Palaeoproterozoic placer deposits. Mineral. Deposita 45, 259–280.

Kojima, S., Sugaki, A., 1985. Phase relations in the Cu–Fe–Zn–S system between 500 degrees and 300 degrees C under hydrothermal conditions. Econ. Geol. 80, 158–171.

Kouzmanov, K., Bailly, L., Ramboz, C., Rouer, O., Bény, J.-M., 2002. Morphology, origin and infrared microthermometry of fluid inclusions in pyrite from the Radka epithermal copper deposit, Srednogorie zone, Bulgaria. Mineral. Deposita 37, 599–613.

Large, R.R., Maslennikov, V.V., Robert, F., Danyushevsky, L.V., Chang, Z.S., 2007. Multistage sedimentary and metamorphic origin of pyrite and gold in the giant Sukhoi Log deposit, Lena gold province, Russia. Econ. Geol. 102, 1233–1267.

Large, R.R., Danyushevsky, L., Hollit, C., Maslennikov, V., Meffre, S., Gilbert, S., Bull, S., Scott, R., Emsbo, P., Thomas, H., Singh, B., Foster, J., 2009. Gold and trace element zonation in pyrite using a laser imaging technique: Implications for the timing of gold in orogenic and Carlin-style sediment-hosted deposits. Econ. Geol. 104, 635–668.

Large, R.R., Halpin, J.A., Danyushevsky, L.V., Maslennikov, V.V., Bull, S.W., Long, J.A., Gregory, D.D., Lounejeva, E., Lyons, T.W., Sack, P.J., McGoldrick, P.J., Calver, C.R., 2014. Trace

element content of sedimentary pyrite as a new proxy for deep-time ocean–atmosphere evolution. Earth Planet Sci. Lett. 389, 209–220.

Larocque, A.C.L., Hodgson, C.J., Cabri, L.J., Jackman, J.A., 1995. Ion microprobe analysis of pyrite, chalcopyrite and pyrrhotite from the Mobrun VMS deposit in northwestern Quebec: Evidence for metamorphic remobilization of gold. Can. Mineral. 33, 373–388.

L'Heureux, I., Fowler, A.D., 1996. Isothermal constitutive undercooling as a model for oscillatory zoning in plagioclase. Can. Mineral., 34: 1137-1147.

Li, N., Deng, J., Yang, Li-Q., Goldfarb, R.J., Zhang, C., Marsh, E., Lei, S-B, Koenig, A., Lowers, H., 2014. Paragenesis and geochemistry of ore minerals in the epizonal gold deposits of the Yangshan gold belt, West Qinling, China. Miner. Deposita 49:427–449

Liu, W., Borg, S.J., Testemale, D., Etschmann, B., Hazemann, J.L. and Brugger, J., 2011. Speciation and thermodynamic properties for cobalt chloride complexes in hydrothermal fluids at 35–440 C and 600 bar: an in-situ XAS study. Geochim. Cosmochim. Acta 75, 1227–1248.

Loftus-Hills, G., Solomon, M., 1967. Cobalt, nickel and selenium in sulphides as indicators of ore genesis. Mineral. Deposita 2, 228-242.

Lorand, J.-P., Alard, O., Luguet, A., Keays, R.R., 2003. Sulfur and selenium systematic of the sub continental lithospheric mantle: Inferences from the Massif Central xenoliths suite (France). Geochem. Cosmochim. Acta 67, 4137-4151.

Lowers, H.A., Breit, G.N., Foster, A.L., Whitney, J., Yount, J., Uddin, M.N., Muneem, A. A., 2007. Arsenic incorporation into authigenic pyrite, Bengal Basin sediment, Bangladesh. Geochem. Cosmochim. Acta 71, 2699–2717.

Mahato, S., Goon, S., Bhattacharya, A., Mishra, B., Bernhardt, H.-J., 2008. Thermotectonic evolution of the North Singhbhum Mobile Belt (Eastern India): A view from the western part of the belt. Precamb. Res.162, 102-127.

Maslennikov, V.V., Maslennikova, S.P., Large, R.R., Danyushevsky, L.V., 2009. Study of trace element zonation in vent chimneys from the Silurian Yaman-Kasy volcanic-hosted massive sulfide deposit (Southern Urals, Russia) using laser ablation-inductively coupled plasma mass spectrometry (LA-ICPMS). Econ. Geol.104, 1111–1141.

Maslennikov, V.V., Maslennikova, S.P., Large, R.R., Danyushevsky, L., Herrington, R.J., Ayupova, N.R., Zaykov, V.V., Lein, A.Yu., Tseluyko, A.S., Melekestseva, I.Yu., Tessalina, S.G., 2017. Chimneys in Paleozoic massive sulfide mounds of the Urals VMS deposits: Mineral and trace element comparison with modern black, grey, white, and clear smokers. Ore Geol. Rev. 85, 64–106.

Mason, B., 1982. Principles of Geochemistry. - John Wiley & Sons, NY, 329 p

Mc Clay, K.R., Ellis, P.G.1984. Deformation of pyrite. Econ. Geol. 83, 1856- 1885.

Measures, C.I., Burton, J.D., 1980. The vertical distribution and oxidation states of dissolved selenium in the northeast Atlantic Ocean and their relationship to biological processes. Earth Planet. Sci. Lett. 46, 385-396.

Meyer, F.M., Oberthur, T., Robb, L.J., Saager, R., Stupp, H.D., 1990 .Cobalt, nickel and gold in pyrite from primary gold deposits and Witwatersrand reefs. South Afr. Geol. 93, 70–82.

Migdisov, A.A., Zezin, D., Williams-Jones, A.E., 2011. An experimental study of Cobalt (II) complexation in Cl− and H_2S-bearing hydrothermal solutions. Geochim. Cosmochim. Acta 75, 4065–4079.

Mishra, B., Pal, N., Ghosh, S., 2003. Fluid evolution of the Mosabani and Rakha copper deposits, Singhbhum district, Jharkhand: Evidence from fluid inclusion study of mineralized quartz veins. J. Geol. Soc. Ind. 61, 51–60.

Misra, K.C., Fleet, M.E., 1974. Chemical composition and stability of violarite. Econ. Geol. 69, 391-403.

Moggi-Cecchi V., Cipriani C., Rossi P., Ceccato D., Rudello V., Somacal H., 2002. Trace element contents and distribution maps of chalcopyrite: a micro-PIXE study. Periodico di Mineralogia 71, 101-109.

Moore, J.N., Ficklin, W.H., Johns, C., 1988. Partitioning of arsenic and metals in reducing sulfidic sediments. Environ. Sci. Technol. 22, 432-437.

Mukhopdhyay, J., Beukes, N.J., Armstrong, R.A., Zimmermann, U., Ghosh, G. Medda, R.A., 2008. Dating the oldest greenstone in India: A 3.51-Ga precise U-Pb SHRIMP zircon age for dacitic lava of the southern Iron Ore Group, Singhbhum craton. J. Geol. 116, 449-461.

Myagkaya, I.N., Lazareva, E.V., Gustaytis, M.A., Zhmodik, S.M., 2016. Gold and silver in a system of sulphide tailings. Part 1: Migration in water flow. J. Geochem. Explor. 160, 16-30.

Nayak, B.K., Panchapakesan, V., 1990. Geothermic control of ore assay in Mosabani mine, Singhbhum-evidences from fluid inclusions. J. Geol. Soc. Ind. 36, 187-194.

Neumayr, P., Walshe, J., Hagemann, S., Petersen, K., Roache, A., Frikken, P., Horn, L., Halley, S., 2008, Oxidized and reduced mineral assemblages in greenstone belt rocks of the St. Ives gold camp, Western Australia: Vectors to high-grade orebodies in Archaean gold deposits?: Mineral. Deposita 43, 363–371.

Nickel, E.H., 1973.Violarite, a key mineral in the supergene alteration of nickel sulfide ores. Perth Conference, Aust.. Inst. Min.Metal., Perth, W. A., Australia, May 1973, 111-116.

Nickel, E.H., Ross, J.R., Thornber, M.R., 1974. The supergene alteration of pyrrhotite-pentlandite ore at Kambalda, Western Australia. Econ. Geol. 69, 93-107.

Ohmoto, H., 1986. Stable isotope geochemistry of ore deposits. Rev. Mineral. 16, 185-225.

Ono, S., Eigenbrode, J.L., Pavlov, A.A., Kharecha, P., Rumble, D., Kasting, J.F., Freeman, K.H.,

2003, New insights into Archean S cycle from mass-independent S isotope records from the Hamersley Basin, Australia: Earth Planet. Sci. Lett., 213, 15–30.

Ortoleva, P., 1990. Role of attachment kinetic feedback in the oscillatory zoning of crystals grown from melts. Earth Sci. Rev. 29, 3-8.

Pal, D.C., Saravanan, S.C., Misra, B., 2008. Involvement of high temperature oxidized brine in pre- shearing hydrothermal alteration: evidence from fluid inclusions in tourmaline in feldspathic schist, Pathargora area, Singhbhum shear zone, eastern India. Sec. Asian Cur. Res. Fluid Inclusions (ACROFI-2), Ind. Inst. Tech., Kharagpur, India, 12– 14, November, 2008, Proceedings, p.131–136.

Pal, D.C., Barton, D.B., Sarangi, A.K., 2009. Deciphering a multistage history affecting U-Cu (-Fe) mineralization in the Singhbhum Shear Zone, eastern India, using pyrite textures and compositions in the Turamdih U-Cu (-Fe) deposit. Mineral. Deposita 44, 61- 80.

Pal, D.C., Trumbull, R.B., Wiedenbeck, M., 2010. Chemical and boron isotope compositions of tourmaline from the Jaduguda U (-Cu-Fe) deposit, Singhbhum shear zone, India: Implications for the sources and evolution of mineralizing fluids. Chem. Geol. 277, 245-260.

Pal, D.C., Chaudhury T., Mcfarlane, C., Mukherjee, A., Sarangi, A.K., 2011a. Mineral chemistry and in situ dating of allanite and geochemistry of its host rock in the Bagjata uranium mine, Singhbhum shear zone, India- Implications for chemical evolution of REE mineralization and mobilization. Econ. Geol. 106, 1155-1171.

Pal, D.C., Sarkar, S., Misra, B., Sarangi, A.K., 2011b. Chemical and sulfur isotope compositions of pyrite in the Jaduguda U (-Cu-Fe) deposit, Singhbhum Shear Zone, eastern India: Implications for sulfide mineralization. Ear. Syst. Sci. 120, 475-488.

Pal, D.C., Rhede, D., 2013. Geochemistry and chemical dating of uraninite in the Jaduguda uranium deposit, Singhbhum Shear Zone, India- Implication for uranium mineralization and geochemical evolution of uraninite. Econ. Geol. 108, 1499-1515.

Pal, D.C., Bhowmik, T., 2015.Petrography and microthermometry of fluid inclusions in apatite in the Turamdih uranium deposit, Singhbhum shear zone, eastern India - An insight into ore forming Fluid. J. Geol. Soc. Ind. 86 (3), 253-262.

Papineau, D., Moizsis, S.J., Coath, C.D., Karhu, J.A., McKeegan, K.D., 2005. Multiple sulfur isotopes of sulfides from sediments in the aftermath of Palaeproterozoic glaciations. Geochim. Cosmochim. Acta 69, 5033-5060.

Penniston-Dorland, S.C., Wing, B.A., Nex, P.A.M., Kinnaird, J.A., Farquhar, J., Brown, M., Sharman, E.R., 2008. Multiple sulfur isotopes reveal a magmatic origin for the Platreef platinum group element deposit, Bushveld Complex, South Africa. Geol. Soc. Am. 36, 979-982.

Penniston-Dorland, S.C., Mathez, E.A., Wing, B.A., Farquhar, J., Kinnaird, J.A., 2012. Multiple sulfur isotope evidence for surface-derives sulfur in the Bushveld Complex. Earth

Planet. Sci. Lett. 337-338, 236-242.

Piña, R., Gervilla, F., Barnes, S.-J., Ortega, L., Lunar, R., 2013. Platinum-group elements-bearing pyrite from the Aguablanca Ni-Cu sulfide deposit (SW Spain): A LA-ICP-MS study. Europ. J. Mineral. 25, 241–252.

Pokrovski, G.S., Gout, R., Schoit, J., Zotov, A., Harrichour, J-E, 1996. Thermodynamic properties and stoichiometry of As (III) hydroxide complexes at hydrothermal conditions. Geochim. Cosmochim. Acta 60, 737-749.

Ramdohr, P., 1969. The ore minerals and their intergrowths. Oxford: Pergamon Press.

Rankin, A,H., Ramsey, M.H., Coles, B., Vanlangevelde, F., Thomas, C.R., 1992. The composition of hypersaline, iron-rich granitic fluids based on laser-ICP and Synchrotron- XRF microprobe analysis of individual fluid inclusions in Topaz, Molegranite, eastern Australia. Geochim. Cosmochim. Acta 56, 67–79.

Reich M, Kesler S.E, Utsunomiya S, Palenik C.S, Chryssoulis S.L, Ewing R.C., 2005. Solubility of gold in arsenian pyrite. Geochim Cosmochim Acta 69:2781–2796

Reich, M., Simon A.C., Deditius, A., Barra, F., Chryssoulis, S., Lagas, G., Tardani, D., Knipping,, J., Bilenker, L., Sánchez-Alfaro, P., Roberts, M.P., Munizaga, R., 2016.Trace element signature of pyrite from the Los Colorados Iron oxide-apatite (IOA) deposit, Chile: A missing link between Andean IOA and Iron Oxide Copper-Gold Systems.Econ. Geol. 111, 743–761.

Rekha, S., Upadhyay, D., Bhattacharya, A., Koojiman, E., Goon, S., Mahato, S., Pant, N.C., 2011. Lithostructural anf chronological constraints for tectonic restoration of Proterozoic accretion in the eastern Indian Precambrian Shield. Precamb. Res. 187, 313-333.

Rieger, A., Marschik, R., Diaz, M., Hölzl, S., Chiaradia, M., Akker B., Spangenberg, J., 2010. The hypogene iron oxide copper-gold mineralization in the Mantoverde district, Northern Chile. Econ. Geol. 105, 1271–1299.

Roy, A., Sarkar, S., Jeyakumar, S., Aggrawal, S.K., Ebihara, M., 2002. Sm–Nd age and mantle characteristics of the Dhanjori volcanic rocks, Eastern India. Geochem. J. 36, 503–518.

Rusk, B.G., Oliver, N.H.S., Cleverley, J.S., Blenkinsop, T.G., Zhang, D., Williams, P.J., Habermann, P., 2010. Physical and chemical characteristics of the Ernest Henry iron oxide copper gold deposit, Australia: Implications for IOCG genesis, in Porter, T.M., ed., Hydrothermal iron oxide. Scientific Communications 755 copper-gold and related deposits: A global perspective: Adelaide, PGC Publishing, 3, 201–218.

Saha, A.K., 1994. Crustal evolution of Singhbhum North Orissa, Eastern India. Geol. Soc. Ind. Mem. 27, 341p.

Sarkar, S.C., 1984. Geology and ore mineralization along the Singhbhum Copper-Uranium Belt, Eastern India. Jadavpur University Press, Calcutta, 263p.

Sarkar, S.C., Deb, M., 1974. Metamorphism of sulfides of the Singhbhum Copper Belt, India:

the evidence from the ore fabric. Econ. Geol. 69, 1282-1293.

Sarkar. S. N., Basu, A., 1986. Chemical compositions of existing sulfides in ores from Central Section, Mosaboni Mines: *in* Geology and Geochemistry of sulfide ore bodies and associated rocks in mosaboni and Rakha Mines sections in the Singhbhum Copper Belt. A Diamond Jubilee Monograph, Sarkar, S. N. and associates, Indian School of Mines, Dhanbad, p. 113-121.

Sarkar, S.N., Ghosh, D., Lambert, R.J.St., 1986. Rb-Sr and Pb isotope studies of the Soda granites from the Mosabani, Singhbhum copper belt, eastern India. Ind. J. Earth Sci. 13, 101-116.

Sarkar, S.N., Saha, A.K., Miller, J.A., 1969. Geochronology of the Precambrian rocks of Singhbhum and adjacent regions, eastern India. Geol. Mag. 106, 1545.

Savage, K.S., Tingle, T.N., O'Day, P.A., Waychunas, G.A., Bird, D.K., 2000. Arsenic speciation in pyrite and secondary weathering phases, Mother Lode gold district, Tuolumme County, California. Applied Geochem. 15, 1219–1244.

Schneider, A., 1975. Sulfur.16E.Abundance in common igneous rocks. In: Wedepohl, K. H., ed., Handbook of geochemistry: Berlin, Springer- Verlag, 16-E-1-16-E-19.

Sengupta, S., Paul, D.K., Bishui, P.K., Gupta, S.N., Chakraborty, R., Sen, P., 1994. A geochemical and Rb–Sr isotopic study of Kuilapal granite and Arkasoni granophyre from the eastern Indian craton. Ind. Miner. 48, 77–88.

Sengupta, S., Ghosh, S.K., 1997. The kinematic history of the Singhbhum Shear Zone. Proceeding of the Indian Academic Science (Earth Planetary Science) 106, 185-196.

Sengupta, N., Mukhopadhyay, D., Sengupta, P., Hoffbauer, R., 2005. Tourmaline-bearing rocks in the Singhbhum shear zone, eastern India: Evidence of boron infiltration during regional metamorphism. Am. Mineral. 90, 1241-1255.

Serranti S., Ferrini V., Masi U., Nicoletti M., Conde, L.N., 2002. Geochemical features of the massive sulfide (Cu) metamorphosed deposit of Arinteiro (Galicia, Spain) and genetic implications. Periodical di Mineral. 71, 27-48.

Shalaby, I.M., Stumpfl, E., Helmy, H.M., El Mahallawi, M.M., Kamel, O.A., 2004. Silver and silver-bearing minerals at the Um Samiuki volcanogenic massive sulphide deposit, Eastern Desert, Egypt. Mineral. Deposita 39, 608-621.

Sindeeva, N.D., 1964. Mineralogy and types of deposits of selenium and tellurium. New York, Interscience, 363 p..

Susak, N. J., Crerar, D.A., 1982. Factors controlling mineral zoning in hydrothermal ore deposits. Econ. Geol., 71, 476-482.

Susak, N. J., Crerar, D.A., 1985. Spectra and coordination changes of transition metals in hydrothermal solutions: implications for ore genesis. Geochim. Cosmochim. Acta 49, 555– 564.

Talapatra, A.K., 1968. Sulfide mineralization associated with migmatisation in the southeastern

part of the Singhbhum shear zone, Bihar, India. Econ. Geol. 63, 156-165.

Tischendorf, G. F., Ungethum, H., 1964. Uberdie Bildungsbedingungen von Clausthalit Galenit und Bemerkungen zur Selenverteilung im Galenitin Abhangigkeit vom Redox potential und vomp H-Wert. Chemie der Erde 23, 279-311 (in German).

Walshe, J.L., Solomon, M., 1981. An investigation into the environment of formation of the volcanic-hosted Mt Lyell copper deposits using geology, mineralogy, stable isotopes and a six-component chlorite solid solution model. Econ. Geol. 76, 246-284.

Watmuff, I.G., 1974. Supergene alteration of the Mt Windarra nickel sulfide ore deposit, Western Australia. Mineral. Deposita 9, 199-221.

Wang G., Wang Z.Q., Shi R., Zhang Y.L., Wang K M., 2015a. Mineralogy and isotope geochemical characteristics for Xiaozhen copper deposit, Langao County, Shaanxi Province and their constraint on genesis of the deposit. Geosci. J. 19, 281-294.

Wang, Y., Han, X., Petersen, S., Frische, M., Qiu, Z., Li, H., Li, H., Wu, Z., Cui, R., 2017. Mineralogy and trace element geochemistry of sulfide minerals from the Wocan Hydrothermal Field on the slow-spreading Carlsberg Ridge, Indian Ocean. Ore Geol. Rev. 84, 1-19.

Waren, J.K., 2016. Evaporites: A Geological Compendium.- Springer International Publishing Switzerland. DOI 10.1007/978-3-319-13512-0_1: 1-1813.

Wedepohl, K.H., 1995. Composition of the continental crust. Geochem. Cosmochim. Acta 59, 1217-1232.

Wilson, J.W.J., Kesler, S.E., Cloke, P.L,. Kelly, W.C., 1980. Fluid inclusion geochemistry of the Granisle and Bell porphyry copper deposits, British Columbia. Econ. Geol., 75, 45–61.

Winderbaum, L., Ciobanu, C.L., Cook, N.J., Paul, M., Metcalfe, A., Gilbert, S., 2012. Multivariate analysis of a LA–ICP-MS trace element dataset for pyrite. Math. Geosci. 44, 823–842.

Yardley, B.W.D., Rochelle, C.A., Barnicoat, A.C., Lioyd, G.E., 1991. Oscillatory zoning in metamorphic minerals: an indicator of infiltration metasomatism. Mineral. Mag. 55, 357-365.

Yamamoto, M., 1976. Relationship between Se/S and sulfur isotope ratios, hydrothermal sulfide minerals. Mineral. Deposita11, 197-209.

Figure Caption

Fig.1. (A) Generalized geological map of the eastern Indian shield (after Saha, 1994) showing the study area around Surda, Singhbhum District, Jharkhand, with a sketch map of India showing the position of Surda; (B) Geological map of the area around Surda Copper deposit, modified after Sarkar (1984); (C) Map of level 5 of surda Copper mines showing hanging wall lode, intermediate lode and footwall lode, stope and sample locations with detailed rock type descriptions along a cross-cut in 5th level of Surda

Mines. Mineral abbreviations stand for biotite (Bt), chlorite (Chl), Feldspar (Fs), Quartz (Qtz), muscovite (Ms), schist (sch), sericite (Ser).

Fig.2. (A) Sketch drawing of biotite-chlorite-quartz schist showing massive replacement vein of sulfide along the foliation plane. Augen-shaped veins of quartz are also present along the major schistosity. Surda mine, 7th level, Hanging wall stope; (B) Exposures of chlorite-quartz schist showing chalcopyrite bands co-folded with host schist. In the right top of the figure, chalcopyrite shows flowage feature; (C) Micro XRF image of polished thin section of mineralized chlorite-biotite-muscovite-sericite schist from the 9th Level of the Surda Mine. Sulfide veins comprising Pyrite IA (Py IA, grains are encircled with dotted closed area), Pyrite IB (Py IB), Py III (grain within white outlined box), magnetite (Mag), apatite (Ap), quartz (Qtz) parallel to the pervasive foliation in the rock. Pyrite IA is subhedral to anhedral, Pyrite IB is elongated in nature, while Pyrite III is rounded. Fine needles of chalcopyrite grains (Ccp-encircled with solid line) are oriented along the foliation in the rock; (D) Sulfide veins comprising, chalcopyrite (Ccp II), pyrrhotite (Po), and pyrite (Py II) parallel to the pervasive foliation in the rock, 7th Level, Hanging wall lode; (E) Photomicrographs in reflected light showing discordant veinlet of Ni-bearing pyrite (Py) + pyrrhotite (Po) + pentlandite (Pn) + Ni-pyrite (Ni-Py) within chalcopyrite (Ccp I).

Fig.3. (A) Photomicrographs in reflected light showing anhedral Pyrite IA (Py IA); (B) BSE image showing euhedral Pyrite IB (Py IB) embedded in Chalcopyrite I (Ccp I); (C) Fractures in pyrite (Py 1B) filled up by chalcopyrite (Ccp I); (D) A monomineralic cluster of subhedral pyrites (Py I) that occur along small discontinuous layers, and are embedded in chalcopyrite (Ccp I) groundmass; (E) BSE image showing subhedral Pyrite I (Py I) with inclusions of uraninite (U, white spots) that occur in a zoned layer in the host pyrite dividing Pyrite IA (Py IA) at core from Pyrite IB (Py IB) at rim; Photomicrographs in reflected light showing (F) Elongated and folded pyrite (Py IB) grain with orthogonal fractures; (G) Etching with H_2O_2 and concentrated HNO_3 reveals polygonal grains in Pyrite I with growth (dotted lines showing by arrows), annealed textures, and triple-point junctions (marked by dotted circles) in few grains; (H, I) Veinlets of pyrrhotite (Po) and Pentlandite (Pn) occurring within chalcopyrite (Ccp I). Tiny lath of molybdenite (Mo) is also present in the lower portion of the chalcopyrite grain near to the pyrrhotite veinlet (H). Numbers on Figures (B, E, F, and G) correspond to the spot numbers of compositional data in Table 2.

Fig.4. Photomicrographs in reflected light showing (A) Elongated Pyrite II (Py II) associated with chalcopyrite (Ccp II) and Ni-pyrite (Ni-Py) containing inclusions of magnetite (Mag); (B) Subhedral Pyrite II (Py II) with corroded margin replaced marginally by Ni-pyrite. Relict rounded to sub rounded grains of Pyrite I (Py I), and poikiloblastic inclusions of chalcopyrite (Ccp II) are present within Pyrite II; (C, D) Pyrite II (Py II) is replaced by Ni-pyrite (Ni Py). Violarite (Vio) occurs at the boundary of

Ni-pyrite (Ni Py) (C), while pentlandite (Pn) occurs at the rim of Ni-pyrite (Ni Py) (D); (E) Pyrite II showing intergranular fractures, revealed after etching with hydrogen peroxide and conc. HNO$_3$. Arrays of each pits forming sub-grain walls (marked by black arrows), indicating the onset of polygonization; (F) Violarite (vio) replacing pentlandite (Pn) at the grain boundary; Photomicrographs in reflected light showing different types of twin lamellae of chalcopyrite (Etched with H$_2$O$_2$:NH$_4$OH): (G) Sharp bending of twin lamellae along with superposition and dislocation of some lamellae; (H) Lanceolate twins with branching and abrupt termination along grain boundaries. Superposed twins also dislocated the earlier sets; (I) Thick to thin Straight parallel sided twin lamellae terminate at any point within the chalcopyrite grain; (J) Euhedral overgrowth of Pyrite III (Py III) on Pyrite I (Py I) core. Chalcopyrite III shows mutual boundary relationship with Pyrite III. BSE images of Pyrite III (Py III) showing (K) The overgrowth of subhedral to euhedral Pyrite III on Pyrite IB. Fracture of the Pyrite III grain occupied by supergene Ni-pyrite (Ni Py); (L) Triple point junctions (white dotted circle) among sub-grains. In the upper portion chalcopyrite (Ccp III) shows mutual boundary relationship with pyrite, while in lower portion, it is marginally replaced by Ni-pyrite (Ni Py) (sample no. U21b). Numbers on (A, B, D, F, and J) correspond to the spot numbers of compositional data in Table 2.

Fig.5. EPMA analyses of pyrite: (A) Fe wt.% vs. S wt.% plots; (B) Co ppm vs. Ni ppm plot for the three compositionally different types of pyrite from the present study, along with average Co ppm vs. Ni ppm plots for the compositionally different pyrites of other sulfide deposits of Singhbhum Shear Zone. Cobalt and Ni concentrations below detection limits are plotted with values of their corresponding detection limit. Horizontal and vertical dashed lines are detection limits. Symbols: Filled circle - Mosabani Mines, Sarkar and Basu, 1986; Star- Turamdih Mines, Pal et al., 2009; Plus- Jaduguda Mines, Pal et al., 2011; Open circle– Rakha Mines, Chowdhury and Lentz, 2017. Microanalytical data for pyrite from Ernest Henry, Australia, and Manto Verde, Chile (IOCG) are shown in fields filled with 10% black (Ernest Henry) and 20% black bar (Manto Verde), data sources for Ernest Henry and Manto Verde : Rieger et al. (2010), Rusk et al.(2010); (C) Fe wt.% vs. Co wt.% plots; (D) Fe wt.% vs. Ni wt.% plots; (E) S wt.% vs. As wt.%, plots; (F) Co wt.% vs. As wt.% plots. Abbreviation: r= Pearson's correlation coefficient.

Fig.6. BSE images showing (A) Pyrrhotite (Po) containing inclusion of Pyrite I (Py IB) and Tellurite (Te, white spots), and associated with Ni-pyrite (Ni Py); (B) Euhedral to subhedral nature of Pyrite IA (Py IA; sample no. U25); Trace elements maps of the same sample of (B) display (C) Patchy zoning in the pyrite showing the distribution of Co with Co- rich rugged core that does not mimic the grain boundary; (D, E) As- and Ni-poor Pyrite IA; (F) BSE image showing subhedral Pyrite IB (Py IB) with inclusions of Uraninite (white spot). In the upper portion magnetite (Mag), and in the lower portion, pyrite partly includes epidote (Ep) (Sample no. U21b).Trace element maps of the same sample display;

(G, H) Systematic compositional zoning of Co, and As in the pyrite in which Co- and As-rich core mimics the grain shape. In the lower portion where this pyrite is intruded by epidote, the concentrations of Co and As are very low. High concentration of Co locally present are marked by arrows (G); (I) Ni-poor pyrite with a thin Ni-rich rim. Locally high concentration of Ni are present which are marked by arrows; (J) Trace element concentration across Pyrite IB; Profile (X-Y) along a length of 1000 μm on the images of X-ray Co, As, and Ni maps from (G- I) shows a Co- and As-rich core compared to the rim, while Ni is present only at the rim. In the core, the points at the fractures show very low concentration of Co. The variations in the absolute concentrations of Co and As throughout the grain can be correlated with fine oscillatory zoning. Numbers in (A, B, and F) correspond to the spot numbers of compositional data in Table 2.

Fig.7.Trace element maps of euhedral pyrites display: (A- F) Oscillatory zoning of Co and As, values decreasing from core to rim. The zoning pattern of Co and As are similar, mimic the grain shape. In (B) core shows highest concentration of As; (G, H) Pyrite in Fig. 4(K) showing relict of Pyrite IB with high concentration of Co and As at the core of euhedral Pyrite III; (I- K) Incipient reverse zoning of Ni showing increasing concentration of Ni towards rim; (L) Total absence of Ni in the both Pyrite IB and III.

Fig.8. BSE image and chemical maps (LA-ICP-MS) of Pyrite I display overgrowth of subhedral Pyrite IB (Py IB) on Pyrite IA (Py IA). Pyrite IB displays partial zoning of Co and As. Nickel (Ni) has dual nature, following the reverse zoning pattern defined by As and Co, and is also enriched along cracks and rims of pyrite grains. Selenium (Se) follows the zoning pattern of Ni. The cracks enriched with Cu, Mn, Hg, Pb, Au, Ag, Sb, Zn, V, Th, and U, transgress the zoning pattern defined by As, Co and Ni. Bismuth (Bi) and Te are positively correlated and occurs along another set of cracks, part of which might belong to the cracks enriched in other elements. Copper, Hg and Ni also occur along cracks which extend from Pyrite IB to core in Pyrite IA. All element concentrations are in ppm.

Fig.9. BSE image and LA-ICP-MS element maps of Pyrite I showing replacement of Pyrite IA (Py IA) by Pyrite IB (Py IB) along rim. Nickel (Ni) and Se show homogeneous distribution in Pyrite IA, while Cu and Hg are heterogeniously distributed throughout the Pyrite IA grain. Cobolt (Co)-, As-rich Pyrite IB also contains Bi and disseminated Cu, Hg, Ni, Sn along rim. All element concentrations are in ppm.

Fig.10. BSE image and LA-ICP-MS element maps of Pyrite IB display partial oscillatory zoning of Co and As. Nickel (Ni) has dual nature, following the reverse zoning pattern defined by As and Co, and is also enriched along cracks and rims of pyrite grains. Enrichment of Mn, Hg, Pb, Au, Ag, Sb, Zn, V, Th, U are along cracks which transgresses the zoning pattern defined by As, Co and Ni. Bismuth (Bi), Cu

and Te are positively correlated and occurs along another set of cracks. Gold (Au) and Ag are disseminated throughout the grain. All element concentrations are in ppm.

Fig.11. BSE image and LA-ICP-MS element maps of Pyrite IB display fine oscillatory zoning of Co and As. Bismuth (Bi), Cu, Ag, Au, Hg, Mn, Pb, Sb, Te, Zn, Ce, Y and U occur both in the rim and fractures. Nickel (Ni) has dual nature, following the reverse zoning pattern defined by As and Co, and also enriched along cracks and rims of pyrite grains which are filled up by other elements. Selenium (Se) shows partial zoning with rim high in concentration of Se than core.

Fig.12. Photomicrographs in reflected light (sample no. U21b): (A) Pyrite II (Py II) at the top showing mutual boundary relationships with chalcopyrite (Ccp II); same pyrite showing spots from where multiple sulfur isotope analysis had been carried out; (B, C) Trace element maps of same pyrite display trace element distribution pattern of Co, and Ni. Pyrite II is locally replaced by Ni- and Co-rich phases at the grain boundary and along micro-cracks; (D- F) Trace element maps of Pyrite III display trace element distribution pattern of Co, Ni, and As. Very low concentration of Co and Ni occur along fractures. In the lower portion Pyrite III is replaced by Co-, Ni-rich Ni-pyrite (Ni Py) (D, E). Very low concentration of As occur throughout the Pyrite III grain (D).
.

Fig.13. LA-ICP-MS element maps of Chalcopyrite display two textures of chalcopyrite, a smooth, clear looking texture- Chalcopyrite I (Ccp I) makes up a large percentage of the grain, while a more porous (?) form- Chalcopyrite II (Ccp II) makes up a narrow percentage along grain boundary. Cobalt, Ni, Hg, Mn, and Pb are heterogeniously distributed within Ccp I, while enrichment of Co, Ni, Mn, Pb, Sb, Hg, and Te occur along rim in Ccp II. In the Ccp II, Ag shows zoning with core rich in Ag than rim portion. Bismuth (Bi) occurs both along fractures of Ccp I and rim of Ccp II. Zinc (Zn) shows grain-scale compositional zoning, increasing from Ccp I to Ccp II with presence of both solid solution and submicroscopic inclusions of sphalerite in Ccp II; Selenium (Se) and Cu are homogeneous throughout the Ccp I and II grains, though a Se-, Cu-rich thin film is present at the rim of Ccp II. All element concentrations are in ppm.

Fig.14. LA-ICP-MS element maps of Chalcopyrite display two types- Chalcopyrite I (Ccp I) and Chalcopyrite II (Ccp II). Similar pattern of Co, Ni, and Bi occur along rim of Ccp II, and also unevenly distributed throughout the Ccp I grain along with Hg, Pb, and Te. The relative concentration of Ag is much higher in the fracture of Ccp I along with Mn, while in Ccp II, Ag concentration increases from core to rim. Selenium (Se), Cu and Zn are homogeneous throughout the Ccp I grain. All element concentrations are in ppm.

Fig.15. (A) Trace element map of Pyrite I displaying trace element distribution pattern of Co, and NanoSIMS analytical spots (sample no. U9) with $\delta^{34}S$ and Co values. The distribution of Co evidences relict growth textures. Dotted line evidences Co-rich core, which records low $\delta^{34}S$ values, while Co-poor rim shows high $\delta^{34}S$ values; Reflected light photomicrographs of the enlarged Pyrite II, Chalcopyrite I and II grains showing (B) Spots of analysis with $\delta^{34}S$, Ni, and Co values of Pyrite II, and $\delta^{34}S$ value of Chalcopyrite II; (C) Spots of analysis with only $\delta^{34}S$ values of Pyrite II and Chalcopyrite II; (D) Chalcopyrite grain (sample no. U41; Ccp I and Ccp II) showing NanoSIMS spot analyses with $\delta^{34}S$ values; (E) $\delta^{34}S$ vs. Cobalt (Co) plot for a single grain of Pyrite I (the spot analyses data of $\delta^{34}S$ and Co values are shown in A).

Fig.16. Interpretive diagram showing the possible sequence of formation of three compositional types of pyrites and chalcopyrites along with sulfidization in the Surda deposit. Abbreviations stand for pyrite (Py), chalcopyrite (Ccp), Pal et al., 2011a, LA- ICPMS U-Pb dating of allanite (1); Mahato et al., 2008, electron probe U-Th-Pb dating of monazite (2); Sarkar et al., 1985, whole rock Rb-Sr age (3); Sengupta et al., 1994, whole rock Rb-Sr age (4).

Highlights
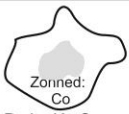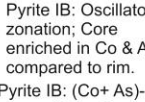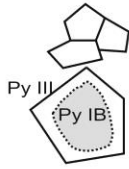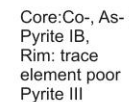
- Petrographic, compositional and sulfur isotope data of pyrite and chalcopyrite from the Surda copper deposit in the Singhbhum Cu-U Belt (India) are significant in building a hydrothermal genetic model.

- All pyrite-chalcopyrite types are early- shearing formed prior to the closing of deformation and metamorphism.

- The source of sulfur for sulfide mineralization might be seawater sulfate and modified seawater.

- The MDF signatures suggest that the mineralization event took place after the great oxidation event.

Table 1
Summery of form, texture and concentration of selected elements of different pyrite types

Types	Shape	Size	Textures	Vein mineral assemblages	Sketches of textures	Co ppm	Ni ppm	Co:Ni (Avg.)	As ppm
Pytrite I	mainly euhedral to anhedral, elongated grains are also present	0.01 to 0.05 mm 0.8 to 2 mm	homogeneous; large porphyroclastic to small heterogeneous grains showing core-rim texture, partial & oscillatory zoning. Elongated grains oriented parallel to mylonitization; etched polygonal grains show annealed texture & triple-point junctions	pyrite I+ chalcopyrite I+ pyrrhotite+ magnetite+ apatite (Concordant Type I vein)	Pyrite IA: Core enriched in Co compared to rim Pyrite IB: Oscillatory zonation; Core enriched in Co & As compared to rim. Pyrite IB: (Co+ As)- rich Pyrite IA: Co- rich	R 5800- 54900 Avg. 18400 R 15000- 31900 Avg. 27000	BDL- 2400 600 BDL BDL	50 -	BDL BDL 300- 13700 7200
Pyrite II	subhedral; small rounded inclusions in Chalco-pyrite I	0.2 to 0.5 mm 0.01 to 0.02 mm	composite, fractured; euhedral, corroded pyrite showing compositional zoning; contains poikiloblastic inclusion of rounded Py IA; etching reveals subgrains & intergranular fractures	1. pyrite II+ pyrrhotite+ pentlandite+ chalcopyrite II ± violarite (Concordant Type 2 vein)	zonned Ni Py IA Pyrite II: Rim enriched in Ni compared to core	R BDL- 8700 Avg. 1600	1200- 37700 7500	0.25	BDL BDL
Pyrite III	small euhedral, rouned	0.01 to 0.03 mm	disseminated unzonned grains; euhedral overgrowths on Py I cores; annealed		Py III Py IB Core:Co-, As- rich Pyrite IB, Rim: trace element poor Pyrite III	R BDL- 700 Avg. 600	BDL- 500 500	1	BDL BDL

Abbreviations: BDL- Below detection limit; Py IA- Pyrite IA; Py IB- Pyrite IB; Py III- Pyrite III

Table 2. Selected EPMA analyses of pyrite, chalcopyrite, and other sulfide minerals from the Surda sulfide deposit

Sample. No.	Rock type	Location	Spot No	S %	Fe %	Co %	Ni %	As %	Cu %	Se %	Total	Mineral	Comment
U 40	Meatbasic rock	Surface	6	53.74	46.71	0.07	1.16	BDL	BDL	BDL	107.68	Pyrite II	Replaced
U 21b	Qtz-Chl sch	5th IL	18	52.13	45.60	0.21	0.86	BDL	BDL	BDL	99.05	Pyrite II	Heterogen
U 21b	Qtz-Chl sch	5th IL	19	52.11	45.00	0.18	3.77	BDL	0.07	BDL	120.13	Pyrite II	Heterogen
U 21b	Qtz-Chl sch	5th IL	20	51.70	44.36	3.19	BDL	1.37	BDL	BDL	120.62	Pyrite IB	Heterogen
U 21b	Qtz-Chl sch	5th IL	21	53.38	45.86	2.28	BDL	BDL	BDL	BDL	100.80	Pyrite IB	Heterogen
U 23	Qtz-Chl sch	5th IL	30	53.27	45.43	1.64	BDL	BDL	BDL	BDL	100.45	Pyrite IA	Heterogen
U 23	Qtz-Chl sch	5th IL	31	53.12	45.62	1.49	BDL	BDL	BDL	BDL	100.24	Pyrite IA	Heterogen
U 23	Qtz-Chl sch	5th IL	33	53.00	41.34	4.68	BDL	2.56	BDL	0.03	101.62	Pyrite IB	Heterogen
U 23	Qtz-Chl sch	5th IL	34	55.13	44.25	2.28	BDL	0.08	BDL	0.03	101.79	Pyrite IB	Homogene
U 26	Fsp sch	5th IL	46	53.77	45.85	0.64	BDL	BDL	0.03	0.02	146.29	Pyrite IA	Heter. euh
U 26	Fsp sch	5th IL	47	53.14	44.76	2.73	0.06	1.10	BDL	0.02	148.79	Pyrite IB	Heter. euh
U 28	Bt-Ms-Qtz sch	5th IL	52	53.67	45.59	0.05	0.07	BDL	0.23	0.31	151.61	Pyrite III	Small roun
U 35	Massive ore	5th FWL	55	53.24	45.25	1.73	BDL	BDL	BDL	BDL	155.22	Pyrite IA	Heterogen
U 35	Massive ore	5th FWL	56	53.18	45.06	1.48	BDL	BDL	BDL	BDL	155.72	Pyrite IA	Heterogen
U 35	Massive ore	5th FWL	57	53.42	45.67	1.32	BDL	BDL	BDL	BDL	157.41	Pyrite IA	Homogene
U 35	Massive ore	5th FWL	60	52.56	45.22	2.83	BDL	BDL	BDL	0.03	160.61	Pyrite IA	Annealed
U 35	Massive ore	5th FWL	61	53.36	45.64	1.52	BDL	BDL	0.11	BDL	100.72	Pyrite IA	Annealed
U 32	Massive ore	5th FWL	68	52.81	45.71	0.07	0.22	BDL	0.06	0.01	166.87	Pyrite II	Replaced
U 32	Massive ore	5th FWL	69	53.69	45.14	0.10	0.73	BDL	BDL	0.02	168.66	Pyrite II	Replaced
U 51	Chl-Qtz sch	10th HWL	79	52.18	44.15	2.78	0.04	BDL	0.16	BDL	178.31	Pyrite IA	Homogene
U 51	Chl-Qtz sch	10th HWL	80	52.18	45.21	2.74	0.05	BDL	BDL	BDL	180.18	Pyrite IA	Homogene
U 43c	Chl-Qtz sch	7th HWL	81	53.32	44.91	0.07	0.12	BDL	BDL	BDL	100.03	Pyrite[*]	Py+Po+Pr
U 43c	Chl-Qtz sch	7th HWL	85	52.50	46.33	0.09	0.20	BDL	0.20	BDL	99.80	Pyrite II	Associated
U 41a	Chl-Qtz sch	7th HWL	89	53.06	45.01	0.95	0.07	BDL	0.14	BDL	100.67	Pyrite IA	Included h
U 41a	Chl-Qtz sch	7th HWL	90	53.51	45.77	0.80	0.05	BDL	0.17	BDL	190.30	Pyrite IA	Included h
U 41a	Chl-Qtz sch	7th HWL	91	53.01	45.97	BDL	0.20	BDL	BDL	BDL	99.76	Pyrite II	Overgrown
U 9	Bt-Ms-Ser sch	9th X-cut	103	52.67	45.21	1.92	BDL	BDL	BDL	0.02	202.80	Pyrite IA	Heterogen
U 9	Bt-Ms-Ser sch	9th X-cut	104	52.07	44.96	2.82	0.03	BDL	BDL	0.04	100.60	Pyrite IA	Heter. elor
U 9	Bt-Ms-Ser sch	9th X-cut	105	53.46	45.50	1.68	0.03	BDL	BDL	BDL	100.73	Pyrite IA	Heter. elor
U 9	Bt-Ms-Ser sch	9th X-cut	106	52.52	46.49	0.04	0.07	BDL	BDL	0.03	205.12	Pyrite III	Small subh
U 9	Bt-Ms-Ser sch	9th X-cut	107	53.83	45.65	1.44	BDL	BDL	0.20	0.20	101.16	Pyrite IA	Heterogen
U 9	Bt-Ms-Ser sch	9th X-cut	108	53.74	45.22	1.54	0.03	BDL	BDL	0.01	100.54	Pyrite IA	Heterogen
U 13	Massive ore	9th HWL	114	50.87	44.47	4.69	BDL	BDL	0.06	BDL	214.09	Pyrite IA	Heterogen
U 13	Massive ore	9th HWL	115	53.44	45.62	1.30	0.05	BDL	BDL	BDL	215.41	Pyrite IA	Heterogen

51

U 13	Massive ore	9th HWL	116	53.33	46.26	0.03	BDL	BDL	0.13	BDL	99.77	Pyrite III	Overgrown
U 41a	Chl-Qtz sch	7th HWL	126	34.32	32.26	0.10	3.10	BDL	29..65	BDL	99.72	Chalcopyrite II	Ccp inclus
U 46a	Chl-Ser-Qtz sch	7th FWL	129	33.14	33.09	0.03	BDL	BDL	31.33	0.03	97.62	Chalcopyrite I	Inclusion-
U 40	amphibolite	Surface	133	32.92	32.66	BDL	0.04	BDL	31.56	BDL	97.24	Chalcopyrite I	Ccp inclus
U 44a	Massive ore	7th HWL	135	33.46	32.42	0.03	0.09	BDL	31.67	BDL	97.73	Chalcopyrite II	Straight bo
U 54	Bt-Qtz sch	3rd HWL	138	23.79	38.09	6.27	27.97	BDL	0.09	BDL	96.30	Violarite	Replacing
U 43c	Chl-Qtz sch	7th HWL	139	23.83	33.30	17.28	21.10	BDL	0.45	BDL	96.35	Ni-pyrite	Py+Po+Pn
U 43c	Chl-Qtz sch	7th HWL	140	62.89	35.33	0.06	0.15	BDL	0.11	BDL	98.90	Pyrrhotite	Py+Po+Pn
U 43c	Chl-Qtz sch	7th HWL	141	27.84	37.78	5.80	26.38	BDL	0.07	BDL	98.55	Pentlandite	Py+Po+Pn
U 35	Massive ore	5th FWL	142	63.07	36.02	0.18	0.35	BDL	BDL	BDL	241.62	Pyrrhotite	Po replacin
U 35	Massive ore	5th FWL	143	27.22	36.71	0.14	30.93	BDL	0.57	BDL	96.03	Ni-pyrite	Adjacent t

Asbbreviations: BDL: below detection limit, Bt: biotite, Ms: muscovite, Chl: chlorite, Qtz: quartz, Ser: sericite, Fsp: feldspathic, sch: schist, Ccp: chalcopyrite, Po: pyrrhotite, Pn: pentlandite, Vio: violarite, Py: pyrite, Ni: Nickel, C: Core, R: Rim, Heter: Heterogeneos, Pyrite[*]: Ni-bearing pyrite in discordant vein

Table 3. Summarized LA-ICP-MS analyses of selected elements of pyrite and chalcopyrite

Sample No.	Spot position	Mineral types	Comments	Fe (ppm)	S (ppm)	As (ppm)	Se (ppm)	Te (ppm)	Co (ppm)	Ni (ppm)	Cu (ppm)	
U9 (1)	Core	Pyrite	Maximum	545726	614113	342	145	49.93	18977	2442	1043	
n= 210		IA	Minimum	390510	453215	58.92	37.95	BDL	5200	412	14.09	
			Mean and	472186	525958	61.99	62.84	0.29	8774	651	40.24	
			±	± 3735	± 4172	34.28.	± 2.09	± 1.07	± 346	± 47.45	± 10.97	
	Subhedral Rim	Pyrite IB	Maximum	543734	590879	2129	204	16.14	12158	3234	1891	
			Minimum	403955	445898	67.83	52.64	0.22	3833	507	11.20	
	n= 106		Mean and	464631	514601	590	96.16	1.52	9371	1238	115	
			±	± 5099	± 5703	± 104	± 4.98	± 0.57	± 308	± 77.50	± 43.78	
U9 (2)	Core	Pyrite	Maximum	527809	528234	3541	180	1748	14946	3978	11119	
	n= 137	IB	Minimum	414468	394557	142	53.43	BDL	4183	457	12.63	
			Mean and	466448	462298	1508	118	31.14	10315	960	696	
			±	± 3713	± 3977	± 148	± 5.54	24.97	± 491	± 55	± 275	
	Between core and rim	Pyrite IB	Maximum	536396	545314	2404	180	74.48	13325	7246	23627	
			Minimum	421763	406435	62.15	50.69	BDL	3484	459	12.04	
			Mean and	466770	458964	1090	115	4.75	9361	1131	847	
	n= 130		±	± 3653	± 3888	94.50	± 5.84	± 1.70	± 299	± 98.63	± 484	
	Euhedral Rim	Pyrite IB	Maximum	497991	496789	1858	141	74.48	11912	2423	30218	
			Minimum	421723	416819	106	46.77	BDL	4169	424	12.29	
	n= 47		Mean and	467524	462876	1708	127	2.41	11467	906	99.29	
			±	± 5776	± 5690	± 126	± 6.44	± 5.74	± 485	± 106	± 1765	
U15	Anhedral Core	Pyrite IA	Maximum	540345	692633	405	164	3.50	15380	450	54.95	
			Minimum	373227	501860	84.43	48.33	0.72	10280	346	0.72	
	n= 41		Mean and	469845	597004	131	101	0.78	12842	391	7.81	
			±	± 11039	± 11730	14.63	± 8.12	± 0.30	± 311	± 8.87	± 3.02	
	Euhedral Rim	Pyrite IB	Maximum	546893	681547	14023	4236	16173	125323	8025	10905	
			Minimum	413550	307875	114	1.28	0.72	11333	92.45	0.89	

52

Sample	Zone	Mineral	Statistic								
	n= 50		Mean and	470116	580751	692	51.44	0.75	15293	114	7.76
			±	± 58238	±20126	± 536	± 164	± 672	± 4343	± 326	± 427
U35	Core	Pyrite	Maximum	527572	595022	575	134	6.08	23569	662	302
	n= 88	IB	Minimum	427094	481859	70	57.70	BDL	16470	343	2.42
			Mean and	468376	534811	212	99.06	0.70	20462	451	22.64
			±	± 4688	± 5754	± 29.02	± 3.72	± 0.24	± 331	± 11.63	± 9.86
	between	Pyrite	Maximum	514546	592585	113	134	21.25	21471	1112	6346
	core and	IB	Minimum	410429	458981	43.54	45.03	BDL	12797	330	2.26
	rim		Mean and	467686	536697	67.85	88.28	2.67	17533	421	531
	n= 130		±	± 3965	± 4529	± 2.58	± 3.74	± 0.85	± 337	± 15.96	± 250
	Euhedral	Pyrite	Maximum	594708	838654	745	374	2671	21300	237718	258620
	Rim	IB	Minimum	431175	399696	12.53	47.02	BDL	5745	78.03	3.25
	n= 85		Mean and	479239	590751	185	114	235	13940	21920	34404
			±	± 5976	±12489	± 30.49	± 12.34	± 89.41	± 1037	± 9726	±10622
U21b	Core	Pyrite	Maximum	541340	678515	6635	125	1.54	36586	1424	460
	n= 118	IB	Minimum	393159	447693	2241	54.30	BDL	19018	342	3.80
			Mean and	468411	522250	3778	88.83	0.32	27234	509	46.82
			±	± 5274	± 6754	± 202	± 2.59	± 0.07	± 589	± 29.88	± 12.41
	Between	Pyrite	Maximum	524071	567712	2293	166	7.29	26294	761	1624
	core and	IB	Minimum	413155	441975	1065	59.54	BDL	18999	380	6.03
	rim		Mean and	465615	506463	1587	94.28	0.51	21676	535	69.76
	n=105		±	± 5088	± 5220	± 48.80	± 4.58	± 0.20	± 284	± 16.90	± 41.60
	Subhedral	Pyrite	Maximum	530767	570542	995	146	17.66	22656	956	2820
	Rim	IB	Minimum	406447	443860	221	46.45	0.00	12572	410	8.00
	n= 46		Mean and	465623	505039	557	94.43	2.44	19044	578	191
			±	± 7670	± 9070	± 67.90	± 7.09	± 1.25	± 726	± 39.34	± 158
U41a	Anhedral	Chalcopyrite	Maximum	353924	546258	1.35	306	17.66	56.73	1022	474932
	Core	I	Minimum	226499	336016	BDL	80.62	0.00	0.36	63	278438
	n= 64		Mean and	305787	448726	0.24	185	3.15	11.15	212	353700
			±	± 74739	±111184	± 0.04	± 44.76	± 0.58	± 0.81	± 28.67	± 84501
	Anhedral	Chalcopyrite	Maximum	462694	716911	58.91	552	20673	309	14606	575167
	Rim	II	Minimum	202923	215112	BDL	80.62	BDL	11.46	119	179304
	n= 72		Mean and	312919	463352	1.57	200	890.83	86.07	2142	343350
			±	± 11075	± 20259	± 1.61	± 18.89	± 24.57	± 16.06	± 683	±17579
U41b	Anhedral	Chalcopyrite	Maximum	365568	584989	274	255	32.42	31	2289	424922
	Core	I	Minimum	275585	428774	165	120	BDL	0.42	78	300064
	n= 118		Mean and	304987	481464	211	186	4.10	4.82	248	345372
			±	± 2024	± 4913	± 3.25	± 5.43	± 0.74	± 1.06	± 60.48	± 3557
	Anhedral	Chalcopyrite	Maximum	481124	537217	2.53	582	180	824	12790	427683
	Rim	II	Minimum	242200	13512	BDL	38.55	BDL	1.15	69	57
	n=73		Mean and	309726	317890	0.38	142	4.53	124	1922	145067
			±	± 6983	± 28935	± 0.17	±17.92	± 4.82	±28.30	± 472	±37858
Average minimum detection		Pyrite		7.94	1572	0.26	1.28	0.26	0.22	0.17	0.30

| limit (MDL) in ppm | Chalcopyrite | 6.67 | 2491 | 0.38 | 2.69 | 0.35 | 0.01 | 0.20 | 4.94 |

Asbbreviations:n= number of spot analyses, BDL: Below detection limit. Notes: ± is 95% Confidence interval

Table 4. Multiple sulfur isotope compositions of sulfide micro-domains analyzed by NanoSIMS

Sample No.	grain spot	Mineral phase	$^{34}S/^{32}S$	± 1σ*	$^{33}S/^{32}S$	± 1σ*	$\delta^{34}S_{CDT}$	± 1σ*	± 2σ*	$\delta^{33}S_{CDT}$	± 1σ*	± 2σ*	$\Delta^{33}S$	± 1σ
U9	a_1	Pyrite IA	0.044413	9.85E-07	0.007901	4.79E-07	5.68	0.022	0.47	3.04	0.061	0.46	0.1	0.0
	a_2	Pyrite IA	0.044399	9.66E-07	0.007899	5.29E-07	5.36	0.022	0.47	2.75	0.067	0.46	-0	0.0
	a_3	Pyrite IA	0.044365	9.17E-07	0.007895	5.55E-07	4.59	0.021	0.47	2.31	0.07	0.46	-0.1	0.0
	a_4	Pyrite IA	0.044335	1.03E-06	0.007892	5.53E-07	3.91	0.023	0.47	1.84	0.07	0.46	-0.2	0.0
							Avg.	4.89		Avg.	2.48		Avg.	-0
							SD	0.79		SD	0.52		SD	0.12
U21b	a_1	Ccp	0.044334	1.08E-06	0.007888	5.45E-07	3.88	0.024	0.47	1.35	0.069	0.46	-0.7	0.0
	b_1	Pyrite II	0.044392	9.89E-07	0.007897	4.88E-07	5.19	0.022	0.47	2.53	0.062	0.46	-0.2	0.0
	b_2	Pyrite II	0.044396	9.22E-07	0.007897	5.15E-07	5.3	0.021	0.47	2.5	0.065	0.46	-0.2	0.0
	b_3	Pyrite II	0.044371	1.03E-06	0.007895	5.44E-07	4.73	0.023	0.47	2.28	0.069	0.46	-0.2	0.0
	b_4	Pyrite II	0.044323	9.96E-07	0.007887	5.25E-07	3.63	0.022	0.47	1.26	0.067	0.46	-0.6	0.0
	b_5	Pyrite II	0.044397	9.13E-07	0.007896	4.97E-07	5.31	0.021	0.47	2.35	0.063	0.46	-0.4	0.0
	b_6	Pyrite II	0.044396	1.02E-06	0.007894	5.29E-07	5.28	0.023	0.47	2.18	0.067	0.46	-0.6	0.0
	b_7	Pyrite II	0.044403	1.03E-06	0.007895	5.35E-07	5.43	0.023	0.47	2.23	0.068	0.46	-0.6	0.0
	b_8	Pyrite II	0.044402	9.62E-07	0.007895	4.95E-07	5.43	0.022	0.47	2.22	0.063	0.46	-0.6	0.0
	c_1	Ccp	0.044388	9.98E-07	0.007887	5.26E-07	5.11	0.022	0.47	1.21	0.067	0.46	-1.4	0.0
	c_2	Ccp	0.044379	1.02E-06	0.007886	5.17E-07	4.9	0.023	0.47	1.13	0.065	0.46	-1.4	0.0
	c_3	Ccp	0.04438	1.02E-06	0.007886	5.17E-07	4.92	0.023	0.47	1.08	0.065	0.46	-1.5	0.0
	d_1	Pyrite II	0.044401	8.59E-07	0.007893	5.56E-07	5.39	0.019	0.47	2.01	0.07	0.46	-0.8	0.0
	d_2	Pyrite II	0.044356	9.12E-07	0.007887	5.15E-07	4.37	0.021	0.47	1.28	0.065	0.46	-1	0.0
	d_3	Pyrite II	0.04438	9.75E-07	0.00789	5.60E-07	4.92	0.022	0.47	1.59	0.071	0.46	-1	0.0
							Avg.	4.92		Avg.	1.81		Avg.	-0.7
							SD	0.56		SD	0.55		SD	0.44
U41	a_1	Ccp	0.044371	1.03E-06	0.007886	5.51E-07	4.71	0.023	0.47	1.17	0.07	0.46	-1.3	0.0
	b_1	Ccp	0.044438	1.04E-06	0.007892	5.44E-07	6.23	0.023	0.47	1.94	0.069	0.46	-1.3	0.0
	c_1	Ccp	0.044368	9.66E-07	0.007885	5.13E-07	4.65	0.022	0.47	0.93	0.065	0.46	-1.5	0.0
	c_2	Ccp	0.044348	1.21E-06	0.007886	5.46E-07	4.21	0.027	0.47	1.11	0.069	0.46	-1.1	0.0
							Avg.	4.95		Avg.	1.29		Avg.	-1.3
							SD	0.88		SD	0.45		SD	0.17

*Errors on isotope ratios and delta values include internal precision (1σ) and external (2σ). The latter is two times the quadratic combination of the internal precision and external reproducibility.
Asbbreviation: Ccp- Chalcopyrite; Avg.- Average; SD.- Standard Deviation

Table 5. Multiple sulfur isotope compositions of microdrilled sulfides analyzed by EA-IRMS.

Sample name/ Analyses #1	$\delta^{34}S_{CDT}$[*]	$\delta^{33}S_{CDT}$[*]	$\Delta^{33}S$[*]	Sample name/ Analyses #2	$\delta^{34}S_{CDT}$[*]	$\delta^{33}S_{CDT}$[*]	$\Delta^{33}S$[*]
U9				U9			
a	5.3	2.5	0.2	a +0.205 mgV$_2$O$_5$	5.8	3.1	0.1
b	5.4	2.5	0.3	b +0.205 mgV$_2$O$_5$	6	3.3	0.2
c	5.5	2.4	0.4	c +0.233mgV$_2$O$_5$	6	3.2	0.1
d	5.1	2.6	0	NS SG+0.571mgV$_2$O$_2$ [$]	6.2	3.2	0
e	5	2.6	0				
f	5.1	2.5	0.1				
Average	5.2	2.5	0.2	Average	6	3.2	0.1
SD	0.2	0.1	0.2	SD	0.2	0.1	0.1
U35				U35			
a	5.2	2.6	0.1	a +0.241mgV$_2$O$_5$	5.4	3	0.1
b	4.8	2.2	0.3	b +0.245mgV$_2$O$_5$	5.7	2.9	0
c	4.7	2.3	0.2	c +0.234mgV$_2$O$_5$	5.7	3	0
d	4.5	2.2	0.1	NS SG+0.257mgV$_2$O$_2$ [$]	6.4	3.5	0.3
e	4.6	2.2	0.2				
Average	4.8	2.3	0.2	Average	5.8	3.1	0.1
SD	0.3	0.2	0.1	SD	0.4	0.3	0.2
U21b				U21b			
a	6	3.1	0	a +0.217mgV$_2$O$_5$	6.5	3.4	0.1
b	5.2	2.5	0.1	b +0.207mgV$_2$O$_5$	6	3.2	0
c	5.7	2.9	0.1	NS SG+0.192mgV$_2$O$_2$ [$]	6.2	3.3	0
d	5.2	2.8	-0.1	NS SG+0.247mgV$_2$O$_2$ [$]	6.1	3.1	-0.1
e	5.8	3	0	NS SG+0.242mgV$_2$O$_2$ [$]	6.3	3.5	0.5
Average	5.6	2.8	0	Average	6.2	3.3	0.1
SD	0.4	0.2	0.1	SD	0.2	0.2	0.2
U41				U41			
a	6.1	2.8	0.3	a +0.261mgV$_2$O$_5$ [$]	6.7	3.4	-0.1
b	6.2	3.1	0.1	b +0.228mgV$_2$O$_5$ [$]	6.8	3.6	0.1
c	5.6	2.6	0.3	c +0.221mgV$_2$O$_5$ [$]	6.5	3.5	0
d	5.7	2.8	0.1	NS SG+0.264mgV$_2$O$_2$ [$]	6.5	3	-0.2
e	5.7	2.7	0.2	NS SG+0.033mgV$_2$O$_2$ [$]	6.6	4	0.6
f	5.7	3	-0.1				
Average	5.8	2.8	0.2	Average	6.6	3.5	0.1
SD	0.2	0.2	0.1	SD	0.2	0.2	0.1

[*]Errors on $\delta^{33}S$, $\delta^{34}S$, and $\Delta^{33}S$ are taken as the 1σ reproducibility on the average of multiple international and in-house standards, which yielded 0.3, 0.4, and 0.2‰.
[$] Analyses performed on powdered single grains analyzed by NanoSIMS, and extracted from the Indium in sample mount
[1] Data from Boston College (no V$_2$O$_5$ used, corrected with CDT and sulfonilamide standards)
[2] Data from Harvard University (V$_2$O$_5$ used, corrected with S1, S2, and S3 standards); SD- Standard Deviation